REPORT DOCUMENTATION PAGE

Form Approved OMB NO. 0704-0188

1. REPORT DATE (DD-MM-YYYY)	2. REPORT TYPE	3. DATES COVERED (From - To)
27-02-2017	Final Report	1-May-2013 - 31-Oct-2016

4. TITLE AND SUBTITLE
Final Report: Measurement and Analysis of Granular Soil Beneath Lightweight Robotic Running Gear

5a. CONTRACT NUMBER
W911NF-13-1-0063

5b. GRANT NUMBER

5c. PROGRAM ELEMENT NUMBER
611102

6. AUTHORS
Karl Iagnemma

5d. PROJECT NUMBER

5e. TASK NUMBER

5f. WORK UNIT NUMBER

7. PERFORMING ORGANIZATION NAMES AND ADDRESSES
Massachusetts Institute of Technology (MIT
77 Massachusetts Ave.
NE18-901
Cambridge, MA 02139 -4307

8. PERFORMING ORGANIZATION REPORT NUMBER

9. SPONSORING/MONITORING AGENCY NAME(S) AND ADDRESS (ES)
U.S. Army Research Office
P.O. Box 12211
Research Triangle Park, NC 27709-2211

10. SPONSOR/MONITOR'S ACRONYM(S)
ARO

11. SPONSOR/MONITOR'S REPORT NUMBER(S)
63595-EG.6

12. DISTRIBUTION AVAILIBILITY STATEMENT
Approved for Public Release; Distribution Unlimited

13. SUPPLEMENTARY NOTES
The views, opinions and/or findings contained in this report are those of the author(s) and should not contrued as an official Department of the Army position, policy or decision, unless so designated by other documentation.

14. ABSTRACT
A simple and efficient methodology to generate a mobility map accounting for two sources of uncertainty, namely measurement errors (RMSE of a Digital Elevation Model) and interpolation error (kriging method) is proposed. This methodology means a general-purpose solution since it works with standard and publicly-available Digital Elevation Models (DEMs). The different regions in the map are classified according to the geometry of the surface (i.e. slope) and the soil type. A novel segmentation-based approach has also been proposed to divide the regions of interest into segments where stationarity is ensured. Finally, an initial investigation has been performed showing the

15. SUBJECT TERMS

16. SECURITY CLASSIFICATION OF:			17. LIMITATION OF ABSTRACT	15. NUMBER OF PAGES	19a. NAME OF RESPONSIBLE PERSON
a. REPORT	b. ABSTRACT	c. THIS PAGE			Karl Iagnemma
UU	UU	UU	UU		19b. TELEPHONE NUMBER 617-955-9893

Report Title

Final Report: Measurement and Analysis of Granular Soil Beneath Lightweight Robotic Running Gear

ABSTRACT

A simple and efficient methodology to generate a mobility map accounting for two sources of uncertainty, namely measurement errors (RMSE of a Digital Elevation Model) and interpolation error (kriging method) is proposed. This methodology means a general-purpose solution since it works with standard and publicly-available Digital Elevation Models (DEMs). The different regions in the map are classified according to the geometry of the surface (i.e. slope) and the soil type. A novel segmentation-based approach has also been proposed to divide the regions of interest into segments where stationarity is ensured. Finally, an initial investigation has been performed showing the major impact that moisture and vegetation produce on a soil and how that effect may be measured using thermal cameras.

Enter List of papers submitted or published that acknowledge ARO support from the start of the project to the date of this printing. List the papers, including journal references, in the following categories:

(a) Papers published in peer-reviewed journals (N/A for none)

Received Paper

TOTAL:

Number of Papers published in peer-reviewed journals:

(b) Papers published in non-peer-reviewed journals (N/A for none)

Received Paper

TOTAL:

Number of Papers published in non peer-reviewed journals:

(c) Presentations

Number of Presentations: 0.00

Non Peer-Reviewed Conference Proceeding publications (other than abstracts):

Received	Paper

TOTAL:

Number of Non Peer-Reviewed Conference Proceeding publications (other than abstracts):

Peer-Reviewed Conference Proceeding publications (other than abstracts):

Received	Paper	
08/25/2014	2.00	P Jayakumar, K Iagnemma, C Senatore. EXPERIMENTAL STUDY OF LIGHTWEIGHTTRACKED VEHICLE PERFORMANCE ON DRYGRANULAR MATERIALS, Intl Society of Terrain Vehicle Systems. 04-NOV-13, . : ,

TOTAL: **1**

Number of Peer-Reviewed Conference Proceeding publications (other than abstracts):

(d) Manuscripts

Received	Paper	
08/25/2015	4.00	Ram‼on Gonz‼alez ┌, Paramsothy Jayakumar ┌, Karl Iagnemma. Stochastic Mobility Prediction of Ground Vehicles over LargeSpatial Regions. A Geostatistical Approach., Autonomous Robots (08 2015)
08/25/2015	3.00	Shingo Ozaki, Kosuke Hinata , Carmine Senatore, Karl Iagnemma. Finite element analysis of periodic ripple formationunder rigid wheels, JOURNAL of terramechanics (05 2015)
08/25/2015	5.00	J.Y. Wong, C. Senatore, P. Jayakumar, K. Iagnemma. Application of the computer-aided method NTVPM to predicting small, lightweight track system performance, JOURNAL of terramechanics (02 2015)

TOTAL: **3**

Number of Manuscripts:

Books

Received Book

TOTAL:

Received Book Chapter

TOTAL:

Patents Submitted

Patents Awarded

Awards

Graduate Students

NAME	PERCENT_SUPPORTED
FTE Equivalent:	
Total Number:	

Names of Post Doctorates

NAME	PERCENT_SUPPORTED
Ramon Gonzales	1.00
FTE Equivalent:	**1.00**
Total Number:	**1**

Names of Faculty Supported

NAME	PERCENT_SUPPORTED	National Academy Member
Karl Iagnemma	0.20	
FTE Equivalent:	**0.20**	
Total Number:	**1**	

Names of Under Graduate students supported

NAME	PERCENT_SUPPORTED
FTE Equivalent:	
Total Number:	

Student Metrics

This section only applies to graduating undergraduates supported by this agreement in this reporting period

The number of undergraduates funded by this agreement who graduated during this period: .....

The number of undergraduates funded by this agreement who graduated during this period with a degree in science, mathematics, engineering, or technology fields:.....

The number of undergraduates funded by your agreement who graduated during this period and will continue to pursue a graduate or Ph.D. degree in science, mathematics, engineering, or technology fields:.....

Number of graduating undergraduates who achieved a 3.5 GPA to 4.0 (4.0 max scale):.....

Number of graduating undergraduates funded by a DoD funded Center of Excellence grant for Education, Research and Engineering:.....

The number of undergraduates funded by your agreement who graduated during this period and intend to work for the Department of Defense .....

The number of undergraduates funded by your agreement who graduated during this period and will receive scholarships or fellowships for further studies in science, mathematics, engineering or technology fields: .....

Names of Personnel receiving masters degrees

NAME
Total Number:

Names of personnel receiving PHDs

NAME
Total Number:

Names of other research staff

NAME	PERCENT_SUPPORTED
FTE Equivalent:	
Total Number:	

Sub Contractors (DD882)

Inventions (DD882)

Scientific Progress

Technology Transfer

Project Summary - Grant # W911NF-13-1-0063
(FINAL REPORT)

Measurement and Analysis of Granular Soil Beneath Lightweight Robotic Running Gear

Dr. Karl Iagnemma
Department of Mechanical Engineering
Massachusetts Institute of Technology, Cambridge, MA, 02139

Objective

The objective of the proposed research is to propose a new methodology for stochastic vehicle mobility prediction over large regions, for integration into a next-generation NRMM.

Approach

A simple and efficient methodology to generate a mobility map accounting for two sources of uncertainty, namely measurement errors (RMSE of a Digital Elevation Model) and interpolation error (kriging method) is proposed. This methodology means a general-purpose solution since it works with standard and publicly-available Digital Elevation Models (DEMs). The different regions in the map are classified according to the geometry of the surface (i.e. slope) and the soil type. A novel segmentation-based approach has also been proposed to divide the regions of interest into segments where stationarity is ensured. Finally, an initial investigation has been performed showing the major impact that moisture and vegetation produce on a soil and how that effect may be measured using thermal cameras.

The proposed framework has the following features:

- Global path planning is considered rather than local path planning (i.e. planning in the close vicinity of the vehicle). From the decision-maker's standpoint, this feature is important because it provides an ability to make movement decisions over large spatial regions.
- The main source of uncertainty comes from surface geometry (elevation). The first one is framed within the context of global path planning;
- The second key element used in the proposed methodology to designate GO/NOGO regions deals with the soil type. In this way, soils that may lead to a high embedding risk or high slip conditions are avoided during the planning step.
- An efficient solution can be obtained and has been demonstrated on a standard-performance computer and through the well-known Geographic Information System (GIS) ArcGIS (ESRI).
- Other experiments have been run by using the Matlab mGstat toolbox. However, this environment led to higher computation times, near one order to magnitude.
- An initial investigation focused on the challenges associated with the use of thermal cameras in wet and vegetated soils shows how thermal properties actually depends on the moisture content.

Techniques

- Digital terrain modeling. We are interested in methods that provide not only the elevation at areas where there is sparse or no data, but also, and most importantly, an estimate of estimation error, that is, the uncertainty associated with that new point. Ordinary Kriging, a known method in the field of Geostatistics, produces an interpolation function based on a covariance or variogram model derived from the data leading to both an estimate of the elevation and the uncertainty associated to it.
- The use of fractal dimension and elevation range metrics have been explored in order to ensure the variogram non-stationarity requirement.
- Mobility map based on the geometry of the surface (i.e. slope) and the soil type (Unified Soil Classification System, USCS). In particular, the stochastic mobility map represents with a specific level of certainty if a region is traversable or not, such threshold is specified by the decision maker (e.g. 70% of the N random realizations a point is classified as GO).
- Route planning. This element deals with finding the optimal route between two points taking into account both the maximum slope that the vehicle can drive over (NOGO cells dealing with slope), and the undesired terrain with high risk of vehicle embedding. A cost-based path planner algorithm (similar to D*) has been implemented. The optimal route is given in terms of several performance indices (e.g. the shortest route, the route with the lowest uncertainty, and the flattest route).
- Thermal inertial. A relation is observed between thermal inertia and traversability (low thermal inertia, low traversability; and vice versa). This result may be considered for maximizing traversability over sandy soils with higher thermal inertias, what eventually means higher compaction and safer routes.
- Stochastic conditional simulation. Rather than producing a single surface with an estimate of predicition error, many realizations of the original surface are generated. These simulated surfaces all have the same values at sampled locations (X-Y axis) but deviate from one another at the elevation (Z axis). Conditional simulation falls in the broad scope of so-called Monte Carlo methods in order to account for the variability of random processes.

Relevance to Army

This research is relevant to the Army because it promises to enable new capabilities in simulation of (unmanned and manned) military vehicles. The proposed stochastic framework will provide decision-makers with the ability to make movement decisions over large (> 5x5 [km^2]) and uncertain spatial regions (variability in the elevation). This contribution is expected to be of high importance to future Army missions, due to decision-makers will be able to obtain a comprehensive and reliable analysis of the mobility capabilities of their vehicles before attempting a mission. The methodology developed in this research means a significant impact on the NATO Reference Mobility Model (NRMM). Notice that previous attempts to convert NRMM from a deterministic framework to a stochastic one have failed in the core component of a stochastic procedure, that is, the origin of uncertainty. No formal mathematical reasoning about the uncertainty introduced in the simulations is given. In addition to that, the (stochastic) solution proposed in the 1990s required supercomputers and demanded an extensive time to obtain a solution.

Novel modeling approaches can also be integrated into dynamics simulation software such as ANVEL (developed by Quantum Signal LLC). High fidelity simulations will improve design and operations of a large class of vehicles. Additionally, the proposed stochastic framework has been implemented and tested in the well-known GIS software ArcGIS developed by ESRI.
Lastly, the initial investigation showing the relation between the thermal properties of a soil and its moisture content will be also welcome in the next-generation NRMM.

Accomplishments

- Stochastic mobility map. The proposed methodology has been validated using a real 26x40-km^2 USGS DEM including soil information: (1) interpolation of the DEM to a finer resolution (30-m to 20-m); (2) analysis of the number of random realizations to account for the variability of the data; (3) efficient computation time (4-million-point DEM requires less than 30 minutes to complete the whole process).
- Route planning using the stochastic mobility map (constraints in elevation and soil properties). The two optimal routes have been found in the previous DEM between two given points. The first route avoids the NOGO regions due to high slope and the NOGO regions due to a high-embedding-risk soil. The second route avoids the NOGO regions due to high slope. The first route has a length of 25 [km], and the second route has a length of 16 [km].
- Route planning considering different performance indices. From a stochastic standpoint the route that minimizes the uncertainty between points is the safest one, however, it is generally the longest route. On the other hand, the route that minimizes the slope between points leads to the less energy-demanding route but more dangerous route (high uncertainty).
- The novel segmentation-based approach has ensured non-stationarity both in natural (i.e. Brownian-like) environments and in man-made environments or a combination of them.
- An initial investigation demonstrates that discrimination between wet-sand, dry-sand, and vegetated areas is possible by means of thermal vision. In particular, surfaces with the highest thermal inertia, wet sand and grass, also meant the most traversable/compact terrains.

Collaborations and Technology Transfer

- We have been actively collaborating with the company SmartUQ in transferring our methodology (implementation, simulations, etc.) to the next phase of the project.
- We have collaborated with the University of Almeria (Spain) in the use of thermal cameras to investigate the relation between thermal properties and soil traversability.
- We have worked with Dr. Sally Shoop from U.S. Army ERDC-Cold Regions Research and Engineering Laboratory in creating mobility maps based on soil uncertainty.
- We have collaborated with Professor J.Y. Wong (Mechanical and Aerospace Engineering Department, Carleton University), with TARDEC involvement (Dr. P. Jayakumar), in considering soil moisture in the Bekker-Wong terramechanics model.

Resulting Journal Publications

- Gonzalez R, Jayakumar P, Iagnemma K. Stochastic Mobility Prediction of Ground Vehicles over Large Spatial Regions. A Geostatistical Approach. Autonomous Robots, Vol. 41, pp. 311-331, 2017.
- Gonzalez R, Lopez A, Iagnemma K. Thermal Vision, Moisture Content, and Vegetation in the Context of Off-Road Mobile Robots. Journal of Terramechanics, Vol. 70, pp. 35-48, 2017.

- Gonzalez R, Jayakumar P, Iagnemma K. Generation of Stochastic Mobility Maps for Large-Scale Route Planning of Ground Vehicles. A Case Study. Journal of Terramechanics, Vol. 69, pp. 1-11, 2017.
- Gonzalez R, Jayakumar P, Iagnemma K. An Efficient Method for Increasing the Accuracy of Mobility Maps for Ground Vehicles. Journal of Terramechanics, Vol. 68, pp. 23-35, 2016.

Additional Supporting Material

The following sections introduce in more detail the contributions previously summarized.

1. Generation of Stochastic Mobility Maps for Large-Scale Route Planning

1.1 General description of the proposed methodology

As already mentioned, the objective of this work is to describe a stochastic framework for vehicle mobility prediction over large regions. The result of this framework is a stochastic mobility map or stochastic GO/NOGO map where regions in the map are labeled according to the mobility features of a given vehicle. In this case, traversability is defined in terms of the maximum slope the vehicle can drive over and the soil features (e.g. high embedding risk or high slip).

Figure 1 shows the proposed methodology. The inputs consist of a USGS DEM of a target environment and the soil information related to the different regions composing such environment. A higher resolution model of such terrain (smoother surface) is determined via the kriging interpolation method. Kriging yields a prediction map and an error map, the latter map quantifies the uncertainty of the elevation at each location. This information is then used for statistical simulation, that is, numerous random realizations of the prediction map are generated in order to account for the variability of the data. Each realization results in a profile map (slope between points) and a mobility map (maximum slope the vehicle can drive over). It bears mentioning the stochastic conditional simulation also accounts for the correlation between points in the model of the terrain. Finally, information about the soil type is added to the process. That information also influences the GO/NOGO labeling process.

Notice that the stochastic mobility map derived from this workflow gives a specific level of certainty that a particular region is traversable or non-traversable. This value of certainty is specified by the decision maker. The three important ingredients of the proposed procedure are: (1) uncertainty in the DEM (RMSE); (2) uncertainty due to the interpolation process; (3) soil regions labeled by the decision maker as traversable or non-traversable (high embedding risk).

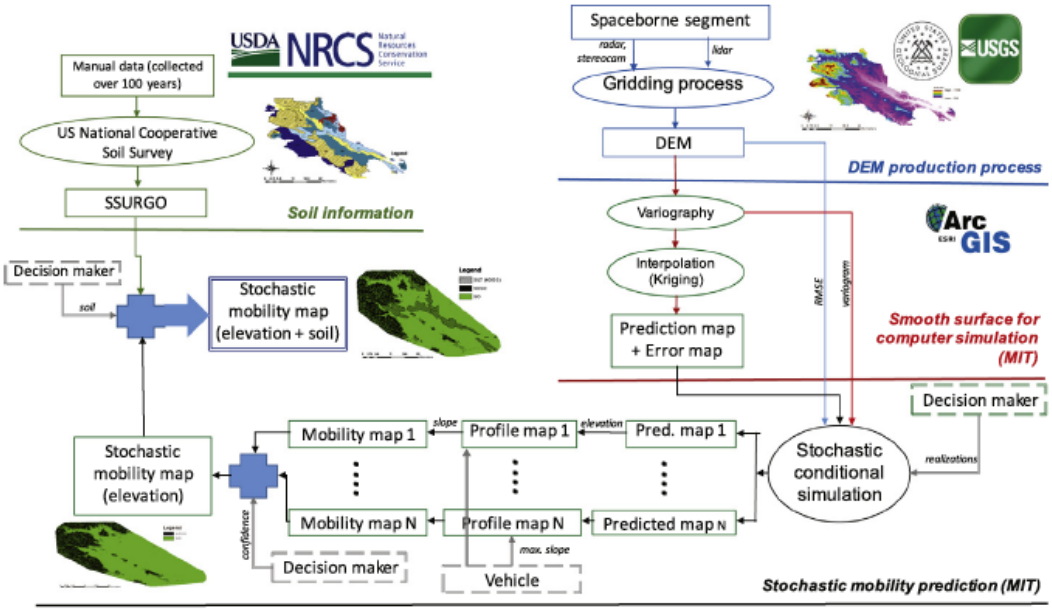

Figure 1. Methodology to obtain a stochastic mobility map considering slope and soil properties

1.2. Stochastic conditional simulation

DEMs consist of a sampled array of elevations for a number of ground positions at regularly spaced intervals. DEMs are generally produced using an interferometric synthetic aperture radar onboard a satellite or using digital image correlation methods.

As already explained, a stochastic conditional simulation is proposed in this work to cope with the uncertainty in the model of the terrain, that is, the spatial variability. Rather than producing a single surface with an estimate of prediction error, many realizations of the original surface are generated. These simulated surfaces all have the same values at sampled locations (X-Y axes) but deviate from one another at the elevation (Z axis). Conditional simulation constitutes a well-known strategy in the context of geostatistics to account for the variability in the data (elevation) derived from kriging interpolation. Additionally, conditional simulation falls in the broad scope of so-called Monte Carlo methods.

One key element in the stochastic conditional simulation is that the randomly generated surfaces must consider the statistical characteristics of the original model of the terrain. More specifically, the random realizations must be obtained considering the autocorrelation or spatial dependence between points, that is, the semivariogram. Another important point to be included in the geostatistical simulation is the RMSE related to the DEM, in addition to the error map derived from kriging. Those two key issues are considered in this work.

1.3. Case study. USGS DEM with USCS soil regions

The scenario considered in this study comprises a region of California called Fort Hunter Liggett (Figure 2). The data is formatted as a USGS DEM with a spatial resolution of 30 meters. It consists of almost one million points. The region covered in this analysis has a size of 26 x 40 [km^2] approximately (~1000 [km^2]). In addition to the elevation, the file contains a layer with the

different soil regions classified according to the USCS (Figure 2d). Specifically, six soil types are paired with 31 regions: CL (lean clay), CL-ML (lean clay and silt), GC-GM (clayey gravel and silty gravel), GM (silty gravel), ML (silt), and SM (silty sand).

The proposed methodology has been implemented in ESRI ArcGIS (version 10.2.2) running on a laptop (Intel Core i7, 3 GHz, 16 MB RAM, MS Windows 7).

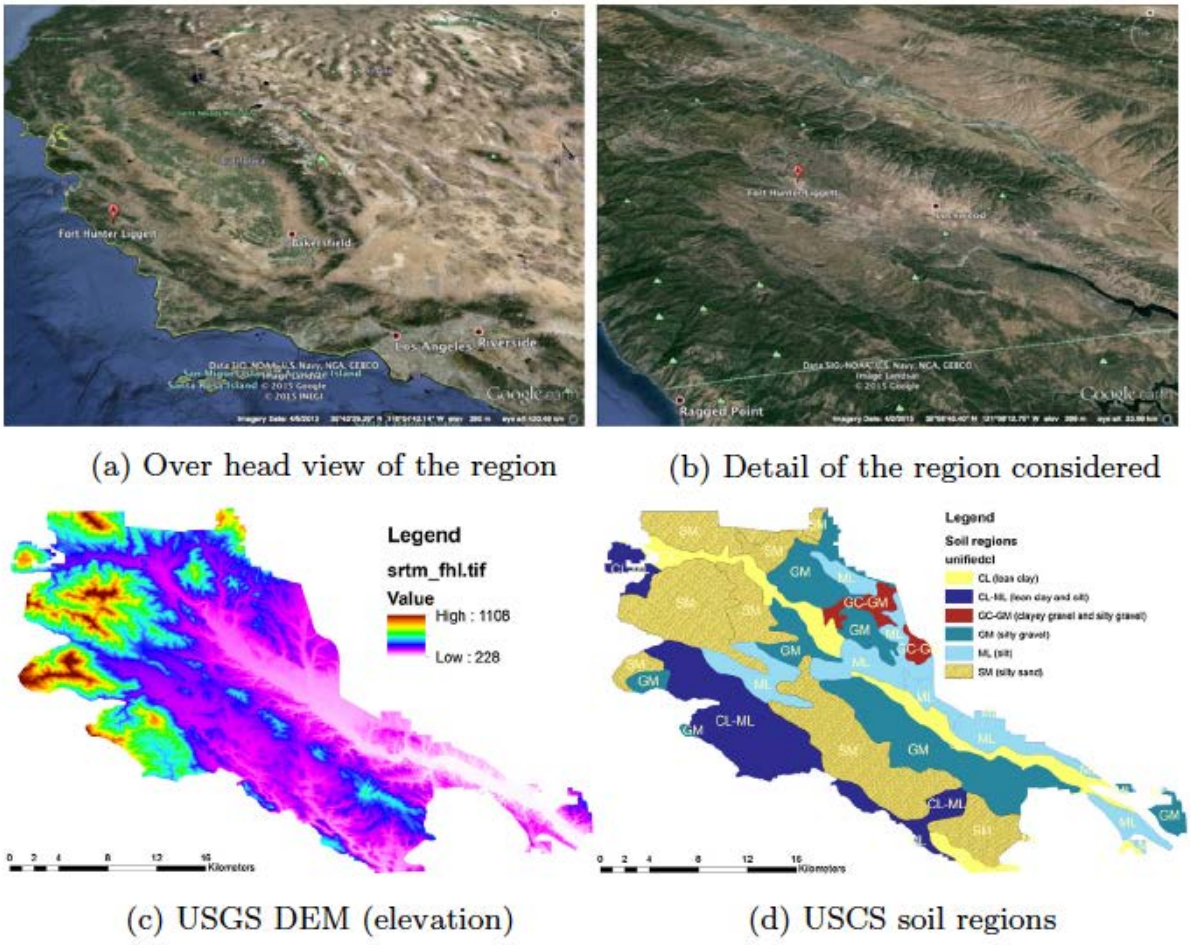

Figure 2. Environment considered in this research (USGS 30-m DEM). Fort Hunter Liggett (CA, USA)

1.3.1. Conversion from geographical coordinates to Cartesian coordinates}

The first step in order to obtain the stochastic mobility map is to convert the initial DEM, in geographical coordinates (Latitute-Longitude), to a more appropriate format, in this case, a Cartesian format, UTM. This process generates a new DEM in Cartesian format: Lambert Conformal Conic (Datum NAD83, Zone 0406, State Plane California). As shown in Figure 3, each location is now formatted in terms of planar coordinates (X-Y) and elevation (GRID_CODE), all of them in metric units.

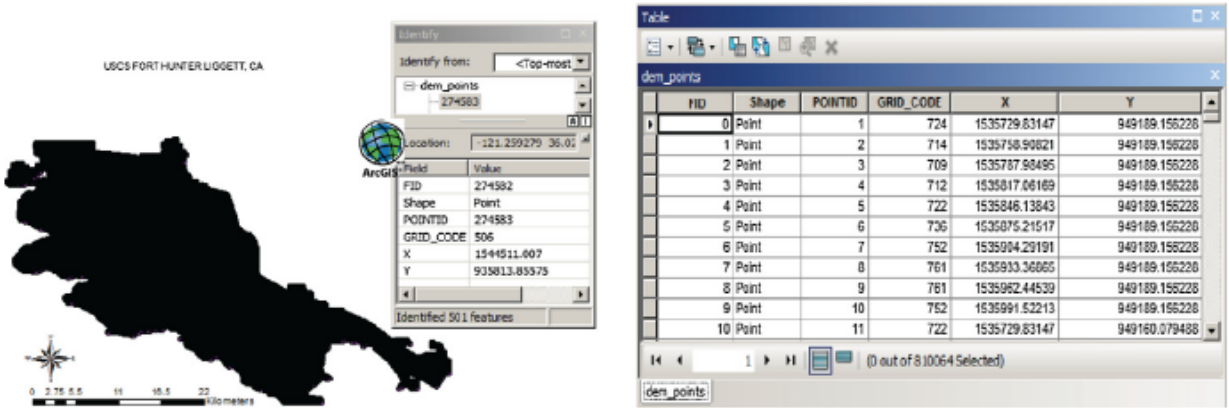

(a) 30-m DEM in Cartesian format (b) Detail of the points in the map

Figure 3. DEM in Cartesian format (UTM, Lambert Conformal Conic, NAD 1983)

1.3.2. Interpolation to a finer resolution. Kriging

1.3.2.1. Interpolation to a finer resolution. Kriging method

As already mentioned, running a reliable computer simulation in the context of mobility prediction needs a high-resolution map. However, current state-of the-art DEMs offer a resolution of 30 meters for US territory and 90 meters for the entire world. In this sense, a downsampling process of the original DEM constitutes a remarkable step before generating the stochastic mobility map. In this work, the original 30-m DEM has been downsampled to a new 20-m DEM, this process has been performed using an interpolation method called kriging. Notice that there is not a consensus in the community about the proper resolution of a map in order to run reliable simulations. For that reason, this value can be easily adjusted in the proposed methodology.

Kriging constitutes a well-known point estimation method in the field of geostatistics. Kriging belongs to Gaussian process regression where the interpolated values are calculated by taking into account a model derived from the own spatial correlation of the data, namely the semivariogram. In geostatistics, this method not only yields a higher resolution surface, but also the estimates of error in those new interpolated points (error map). These features can then be applied to statistical simulation since each interpolated point has associated an uncertainty (kriging variance).

Figure 4 shows the result obtained after applying kriging to the original 30-m DEM. Now, a new 20-m DEM is obtained. Figure 4a shows the semivariogram required to perform kriging. The dots represent the empirical semivariogram, the line is the fitted theoretical semivariogram (i.e. spherical model), and the crosses mean the RMSE between both semivariograms. Figure 4b and Figure 4c show the error map (kriging variance) and the new DEM generated after applying kriging. Notice the small standard deviation observed in the error map. This is not altogether unexpected due to the required downsampling process of 10 meters (30-m to 20-m maps). Larger values will lead to higher uncertainty. Additionally, it is important to observe that the shape of the map is slightly different from the original map. In this case, a polygonal shape has been

selected for two reasons: (1) it is much more efficient to work with these regular shapes than with irregular shapes like in the original map; (2) it is easier to understand the meaning of the kriging variance or uncertainty, as observed in Figure 4b the areas far from the original map have a much higher uncertainty (red regions).

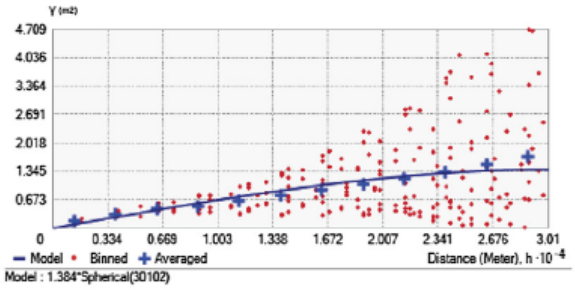

(a) Semivariogram model related to the 30-m DEM

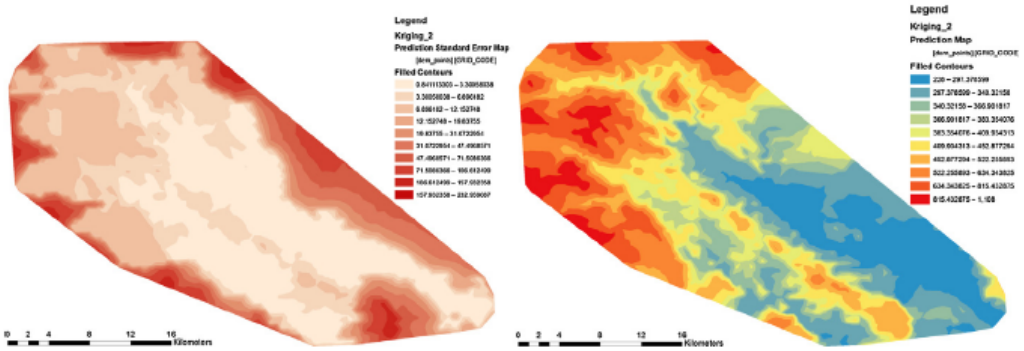

(b) Prediction standard error map. Notice the small standard deviation (uncertainty) within the region defined by the original map

(c) Prediction map (elevation). Notice that the elevation is similar to that found in the original DEM (see Fig. 2c)

Figure 4. New model of the terrain after applying kriging

1.3.2.2. Stochastic conditional simulation

Once kriging is applied, a new model of the terrain is obtained to a finer resolution. The prediction error associated with each point is used for generating a set of random surfaces in order to account for the spatial variability of the data. As previously explained, the methodology suggested in this work considers two sources of uncertainty related to USGS DEMs, that is, the RMSE of USGS DEMs and the error derived from the interpolation process. In this work, a RMSE of 5 m is assumed for the DEM. Additionally, this step considers the spatial correlation between points, that is, the semivariogram previously obtained.

Observe that a key element related to any Monte-Carlo-based simulation is the number of random realizations required to properly represent the variability of the data. In this sense, one way to proceed is to compare a metrics for different number of realizations, and to check when such metrics stabilizes. In the context of this work, a proper metrics is the number of points labeled as GO versus the number of NOGO points. Table 1 summarizes four experiments where various number of random realizations are tested. In this case, two different thresholds have been considered for creating the stochastic mobility map. In the first case, a point will be labeled as

GO if it has been labeled as GO more than 50 \% of the random realizations (e.g. more than 5 times when 10 realizations are tested). As observed, in the second and third columns the number of GO/NOGO points stabilizes when ten or more random realizations are run. Additionally, notice that the mean of those experiments are similar. Another element in this table is the computation time required to generate the random surfaces. This point is also meaningful because using ten realizations instead of 26 or 40 a significant computation time is saved (e.g. 15 minutes versus 20 minutes or 40 minutes).

Table 1
Statistical data related to the experiment to determine the appropriate number of random realizations.

No. of realizations	No. GO points	No. NOGO points	Mean, Std	Time GGS (min)
		Threshold = 50%		
6	3,232,088	926,452	0.78, 0.42	13
10	3,012,989	1,145,551	0.72, 0.45	15
26	3,036,906	1,121,634	0.73, 0.44	20
40	3,058,012	1,100,528	0.73, 0.44	40
		Threshold = 70%		
6	2,793,187	1,365,353	0.67, 0.47	13
10	2,371,982	1,786,558	0.57, 0.49	15
26	2,505,469	1,657,071	0.60, 0.49	20
40	2,407,491	1,751,049	0.58, 0.49	40

Figure 5 shows a comparison between the original DEM and one of the random realizations. As observed in the histogram the number of points (count) is higher in the second case since a higher resolution is set (more than four million points). The mean value is certainly similar (453.75 versus 465.67 [m]). This is not altogether unexpected since the random realization is generated using the semivariogram. In any case, the slight difference is also explained because the RMSE is taken into account in order to generate the random realization.

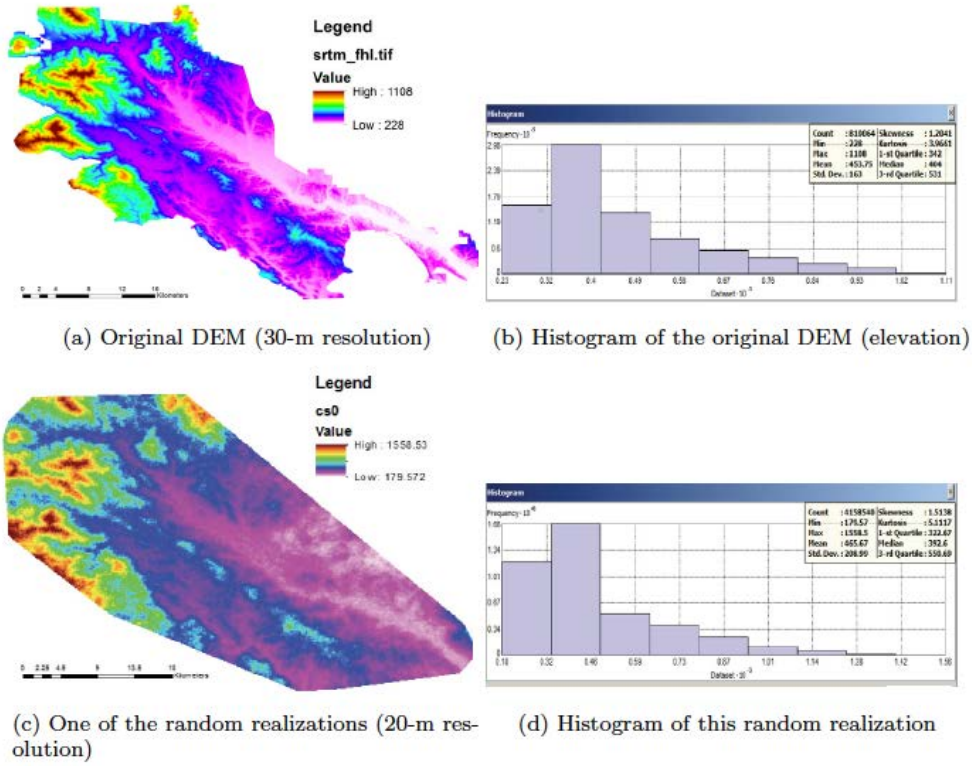

(a) Original DEM (30-m resolution)

(b) Histogram of the original DEM (elevation)

(c) One of the random realizations (20-m resolution)

(d) Histogram of this random realization

Figure 5. Comparison of the original DEM with one random realization of the surface

(elevation)

1.3.2.3. Stochastic mobility map considering slope constraints

Once a set of random realizations of the original surface have been obtained, the next step deals with determining a mobility map. This map shows the traversable and non-traversable regions or GO/NOGO regions depending on the maximum slope the vehicle can drive over. In this case, 20 degrees has been considered as this maximum slope.

Firstly, a slope profile is calculated for each random realization. This slope profile is calculated considering the slope between the 8 neighbor points around a given point. The maximum change in the elevation is then saved in the new slope map, see Figure 6a. After that, those points with a slope less than a given threshold (in this case 20 degrees) are classified as traversable (1) and the remaining points as non-traversable (0), see Figure 6b. Afterwards, all those slope maps are added in order to determine the number of times that a point has been labeled as traversable or non-traversable. Finally, the stochastic mobility map is created accounting for the number of times that a point was labeled as traversable and the ratio specified by the decision maker (e.g. one point is labeled as GO when it is traversable more than 7 out of 10 times).

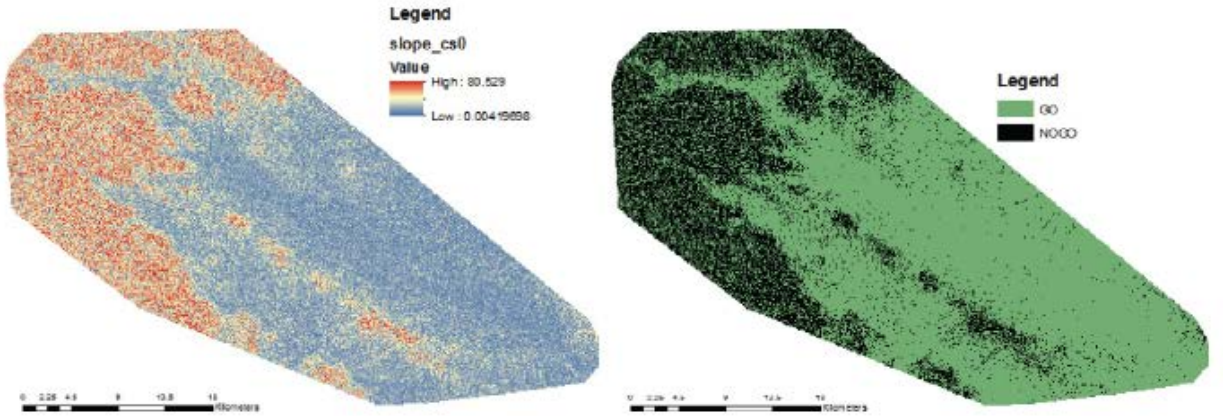

(a) Profile map: this map shows the maximum slope between neighbor points

(b) Mobility map: a point is labeled as GO if slope is less than 20 degrees

Figure 6. Profile map and mobility map of one random realization. This result will be combined with all the random realizations in order to create the stochastic mobility map

1.3.2.4. Stochastic mobility map considering soil constraints

The second key element used in the proposed methodology to designate GO/NOGO regions deals with the soil type. In this particular case, there are six different soil types: CL (lean clay), CL-ML (lean clay and silt), GC-GM (clayey gravel and silty gravel), GM (silty gravel), ML (silt), and SM (silty sand). In this work, the less traversable soil type is assumed silt (ML). The reasoning is explained subsequently.

Typically soils belonging to the category ML include very fine sands, rock dust, and silty or clayey fine sands or clayey silts with slight plasticity. Those properties make that moving over silty soils may lead to a high embedding risk or high slip conditions. This fact is also noticeable in CL (lean clay) since it also belongs to the category of fine-grained soils. However, the cohesion of ML is slightly smaller than CL, which ultimately may mean a higher embedding

risk. In any case, the trafficability of a terrain also depends on the moisture content and other factors (e.g. wheels, mechanical structure, etc.). Thus, not a clear statement can be made using only the soil type. In any case, as a proof of concepts of the methodology suggested in this work, silt (ML) has been assumed as the less traversable soil type and, hence, it must be avoided in the mobility map.

Figure 7a shows the regions that must be avoided (black dots), that is, the regions of the silty soils. The mobility map previously obtained is now updated with those regions, see Figure 7b.

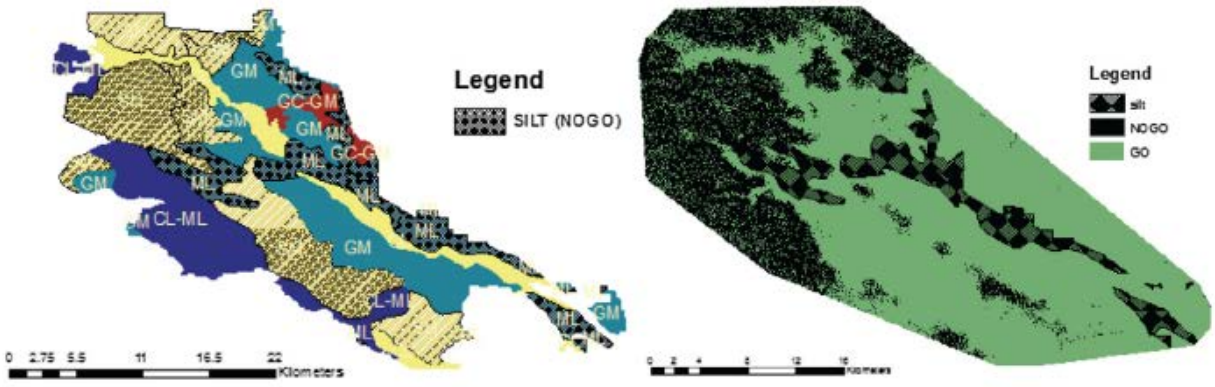

(a) USCS soil regions and silty soils

(b) Mobility map considering undesired soil regions (silty soils)

Figure 7. Selection of those regions with silty soils. These regions are labeled as NOGO in the mobility map

1.3.2.5. Route planning using the complete stochastic mobility map (slope and soil type)
Once the stochastic mobility map has been created taking into account both the maximum slope that the vehicle can drive over (NOGO cells dealing with slope), and the undesired terrain with high risk of vehicle embedding (silty soils), the next step concerns the route planning problem.

In this work, a cost-based path planner algorithm (similar to D*) is used where NOGO cells have a much higher cost (i.e. 100) than the GO cells (i.e. 0.01). In this sense, the optimal route between two points minimizes such cost and avoids the undesired regions of high embedding risk.

Figure 8 shows two routes between one starting point, located in the coordinates (-121.169843, 35.863335)dd, and two different goals, located in the coordinates (-121.246456, 35.998166)dd and (-121.185817, 35.945670)dd, respectively. As expected, the two routes mean the shortest route between the starting and the goal points and the NOGO regions are avoided. In particular, the first route avoids the NOGO regions due to high slope and the NOGO regions due to the silty soil. The second route only needs to avoid the NOGO regions due to high slope. The first route has a length of 25 [km], and the second route has a length of 16 [km].

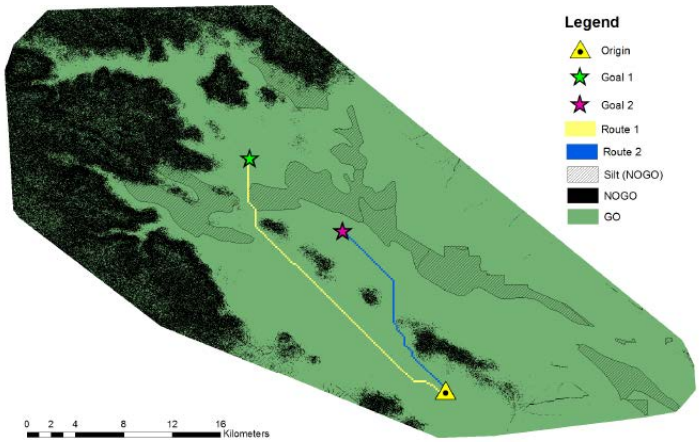

Figure 8. Route planning using the stochastic mobility map. Two different routes are tested each of them avoids NOGO regions related to elevation (slope) and soil type

1.4. Conclusions

This work has been entirely implemented in the well-known software suite ArcGIS developed by ESRI (version 10.2.2). The code has taken advantage of many utilities of the Geostatistical extension. One of the main advantages of this decision is that this methodology and code can be generalized and used for many purposes and input sources. The second advantage accounts for the relatively low computation time (less than 30 minutes for this study of more than 4-million points). Similar results obtained by the authors in Matlab using the mGstat toolbox led to more one order of magnitude higher computation times.

Notice that due to the generality and the flexibility of the methodology contributed in this work, various improvements can be easily integrated. One interesting point is to use the level of uncertainty in the elevation to classify GO/NOGO points. This will add a new degree of freedom to the decision maker to determine the most traversable and safer route.

One limitation of this work and which is motivated by the point mentioned in the first paragraph is that the function used for running the stochastic conditional simulations can only be applied using “Simple Kriging”. This consideration leads to a higher prediction error than using the popular “Ordinary Kriging”. However, this point does not influence the methodology proposed in this work since one function can replace the other when it is updated in ArcGIS.

Another interesting point is that the function used to run Kriging requires a global semivariogram. This assumption is valid when there is a certain spatial homogeneity in the data. However, such as demonstrated in several references, this issue has to be solved using local semivariograms instead of only one global semivariogram. This point also constitutes one of the future efforts to extend the proposed methodology.

There is not a clear answer to what is the most appropriate spatial resolution in order to perform a reliable stochastic mobility prediction analysis. It is not known whether any detailed study on this issue has been performed. It appears that spatial resolution of data for 3D terrain models should be dependent on the size of the vehicle, the variability of the terrain, and on the nature of any natural or man-made obstacles that the vehicle must negotiate. This constitutes an open

question to the whole community. In any case, in this work, the new resolution of 20-m has been considered as a proof of concepts.

As explained along this work, one of the main features of the proposed methodology is that it allows the use of publicly-available DEMs. In the study case addressed here, a USGS 30-m DEM has been employed. In addition to that, the authors plan to test this methodology with state-of-the-art DEMs coming from the recent 3D Elevation Program (http://viewer.nationalmap.gov/viewer) (3DEP). 3DEP is led by the USGS National Geospatial Program, its primary goal is to collect 3D elevation data in the form of LIDAR data over US territories. Because of this new technology, LIDAR, high-resolution (meter to sub-meter scale) maps are available. On the other hand, these elevation maps can be matched with soil information using the USDA National Cooperative Soil Survey (http://websoilsurvey.sc.egov.usda.gov) (NRCS). NRCS has soil maps and data available online for more than 95 percent of the US territory.

2. Stochastic Mobility Prediction of Ground Vehicles over Large Spatial Regions

2.1 General description of the proposed methodology

The first problem addressed in this work is framed within the context of estimating the values of a regionalized variable (elevation) at places where it has not been measured and, after that, analyzing the performance of a vehicle over such terrain.

Figure 1 shows the methodology followed in this research. Initially, a DEM is obtained via a subsampling approach. This is required in order to enable an affordable computation of the variogram and kriging method. Once a set of representative points, in terms of the variogram and elevation profile, are selected, the ordinary kriging method is applied. This procedure yields a model of the terrain at a finer resolution (see Assumption 1). This model can be applied to statistical simulation because each interpolated point has an associated uncertainty (kriging variance). Next, the D* algorithm is applied in order to obtain multiple routes between two points (i.e. starting point and desired goal or waypoint). Finally, the optimal route is given in terms of some performance indices (e.g. the shortest path, the path with the lowest uncertainty, the flattest route, etc.) (see Assumption 2).

Assumption 1 We assume that there is no uncertainty or error associated to the original DEM of the terrain (positional errors, data precision, etc.). In this work, uncertainty in elevation comes only after obtaining a model of the terrain at a finer spatial resolution (new interpolated points), that is, after applying kriging.

Assumption 2 It bears mentioning that the known Humvee military vehicle has been considered as the testbed in this research. The reasoning behind the spatial resolution of the model of the terrain and the use of a car-like kinematic model in the simulations are both based on the dimensions and features of such vehicle.

The main features and limitations of this approach can be summarized as follows:

- Global path planning is considered rather than local path planning (planning in the vicinity of the vehicle). The latter problem is mainly related to detection and avoidance of local obstacles using onboard sensors. In this sense, this research does not ensure local obstacle avoidance. It is assumed that a lower layer to the one proposed here will be available in the real vehicle.
- This solution does not result in a binary answer, i.e. the path is traversable or not; instead statistical data supporting each decision is given.

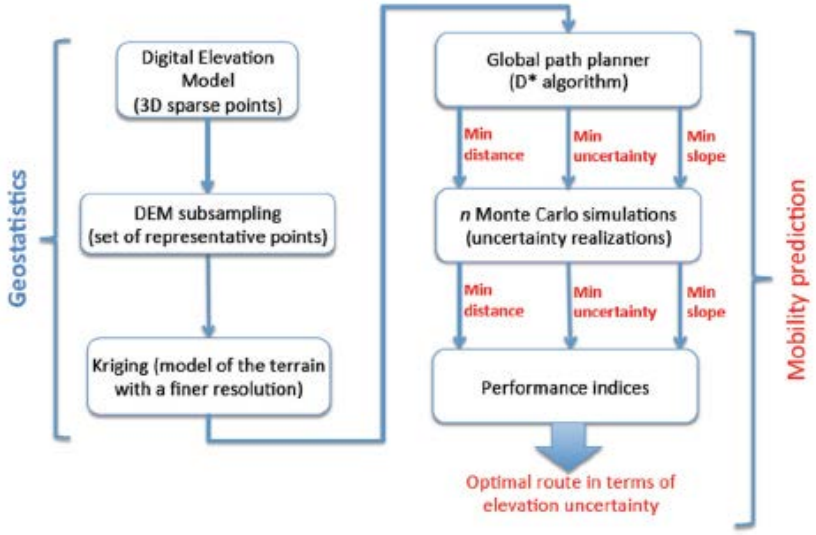

Figure 9. Schematic view of the steps carried out in this research for predicting the mobility of a ground vehicle over a large region (> 5x5 [Km2])

2.2. Reconstruction of a 3D Terrain Surface from Remote Data. Spatial Prediction Problem

The use of geostatistical tools is motivated because the original DEM has a resolution that is too coarse for vehicle mobility prediction (> 30 meters). Thus, an interpolation strategy is required in order to obtain a model of the terrain at a finer resolution. In our case, the desired resolution is the double of the vehicle length, that is, 10 meters (Humvee's length is 5 meters). The most common approach is ordinary kriging, which estimates the elevation of points (at a finer resolution) depending on the elevation and spatial arrangement of measured points (variogram). However, before attempting kriging, a subsampling step is required in order to reduce the number of points of the original DEM. This step is necessary to perform efficient geostatistics-related computations on a standard-performance computer (as remarked in the introductory section).

It bears mentioning that in this research DEM of the terrain are employed. Since the dimensions of the grid are known and the number of observations in each row is known, the implicit spatial relationships between elevation values can be determined. There are mainly two types of DEM depending on the coverage and on the resolution. The US Geological Survey (USGS) agency produced a DEM with coverage of the US with a resolution of 30 meters. A worldwide coverage is offered by the SRTM NASA and NGA agencies. The SRTM DEM have a resolution of 90 meters.

2.2.1. Subsampling a DEM

The reliability of an experimental variogram is affected by the number of samples or its inverse, the density of data. Evidently when all the points of the DEM are considered, the variogram is obtained precisely. However, by increasing the number of samples the computation time required for calculating the variogram (and the subsequent Kriging-based interpolation) increases as well. In this sense, this section proposes a methodology that reduces dramatically the computation time for calculating a variogram despite a high correlation with respect to the variogram obtained if all the point of the DEM were employed (see Remark 1).

*Remark 1*As remarked in the introductory section, one key requirement of the proposed approach deals with an efficient computation. Efficiency is understood in terms of being able to run the proposed methodology in a COTS computer in a reasonable computation time. The reason why the subsampling step has been added to this methodology is because when the variogram and ordinary kriging functions were run over the entire datasets, the computer ran out of RAM memory. After adding this subsampling step, before running kriging, we were able to successfully apply kriging and at a reasonable computation time (around 1-2 hours depending on the size of the environment considered).

2.2.1.1. Systematic Sampling

The systematic sampling method arranges the population according to some ordering scheme and then selecting elements at regular intervals \cite{THO12}. This strategy matches properly with the structure of a DEM, and with the research addressed here. Recall that in a DEM information is recorded at regularly spaced intervals (raster form). For example, if a USGS DEM sampled with a resolution of 30 meters is considered, a sample would be selected every 30 meters.

2.2.1.2. Stratified Sampling via K-Means Algorithm

The stratified sampling approach is based on partitioning a given population into homogeneous subgroups or ``strata". Each stratum is then sampled as an independent sub-population, out of which individual elements can be randomly selected. The principle of stratification is to partition the population in such a way that the units within a stratum are as similar as possible.

The major concern regarding the stratified sampling approach is how to separate the original DEM into different strata. In our context, one reasonable approach is to find such strata depending in elevation. However, this issue is not simple because of the continuous nature of the elevation, especially in uneven terrain. To solve this problem, K-means clustering has been considered. In such publications, K-means is mainly used for stratifying a large region into similar areas mainly in terms of habitat type and soil type. Here, the K-means algorithm is used to split the DEM in terms of elevation. After that, one or two points are randomly selected within each strata. Figure 10 shows the application of the proposed stratified sampling method to the two scenarios considered in this research.

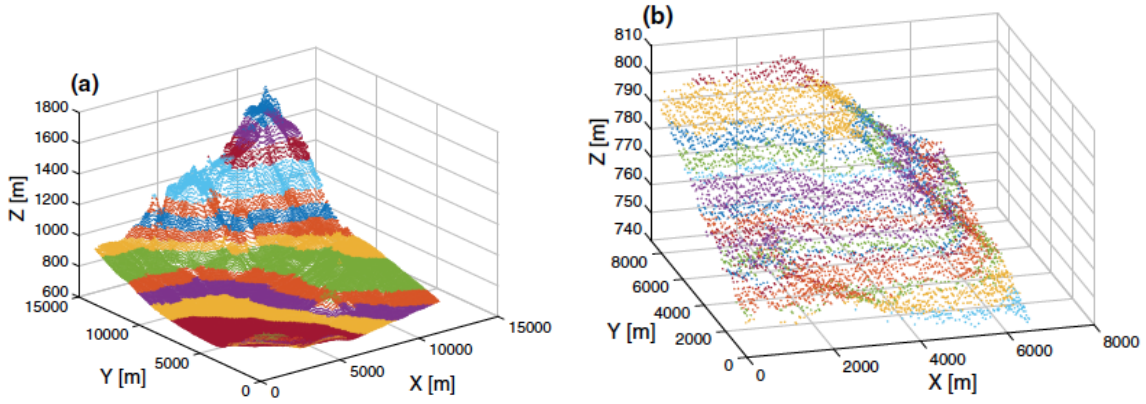

Figure 10. Stratification of two types of DEM. The first one deals with a 30-m resolution DEM and the second example is related to a 90-m resolution DEM. Colors represent different layers or strata.

The key issue of this approach deals with the number of centers used by the K-means algorithm. This is a major issue related to any kind of algorithm based on K-means. In this work, the optimal value is obtained according to the theoretical variogram fitted to the DEM (explained subsequently).

2.2.1.3. Proposed Methodology: Combining Systematic and Stratified Sampling

Recall that the goal of the subsampling approach is to find the minimum number of samples required such that the variogram of this reduced DEM fits the theoretical variogram of the raw DEM. In order to solve this issue, the properties of the variogram and the sampling methods must be taken into account.

First, the variogram is calculated. To obtain a meaningful set of samples the reduced data set should be as sparse as possible in order to cover the whole range of distances in the original DEM. If this fact is not ensured, the variogram would not fit properly the sill. On the other hand, the set of samples should comprise the range of elevations presents in the original DEM as much as possible. This issue has an effect on the range of the variogram. Additionally, we are interested in fitting the elevation profile in order to obtain a meaningful model after applying the Kriging process.

One proposal of combining systematic and stratified sampling approaches is motivated by the following fact. Notice that the systematic sampling approach leads to a sparse set of samples, which cover the entire dataset (Figure 11a). This feature is not found using the stratified sampling approach (Figure 11b). In fact, many samples are clustered at the top right corner. This is explained because of the hill in the environment. Recall that the stratified sampling approach deals with getting samples regarding the different strata (elevations) in the environment, those strata are mainly present in the hill. On the other hand, the stratified sampling approach captures properly the elevations in the original DEM as observed in Figure 10a, but the systematic sampling approach has a worse result in terms of representing the terrain profile (i.e. elevations) (see Table 2). A filter has been implemented to remove those samples that are very close, and hence, to avoid redundancy in the samples.

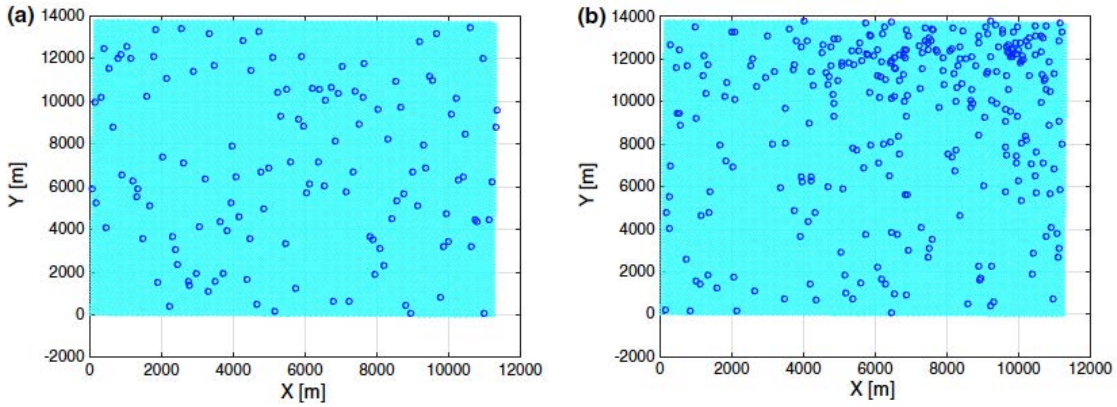

Figure 11. Samples obtained after applying the systematic and stratified sampling approaches to one of the scenarios considered in this work (Death Valley, CA, USA)

2.3. Illustrative Examples

2.3.1. Environments

In order to validate the methods proposed in this research, two different scenarios have been analyzed. First, a region of the Death Valley called Airport Lake (LAT: 35 52 30 N; LONG: -117 37 30 W), see Figure 12. The data were obtained in the 7.5-Min USGS format. This region covers an area of 11.34x13.65 [Km2]. It is important to mention that this DEM is represented in projected coordinates (i.e. UTM system). On the other hand, a region of the Sahara desert in Chad (Africa) has also been considered (LAT: 15 01 67 N; LONG: 21 16 50 E), see Figure 13. The data were obtained in the SRTM format. This region covers an area of 6.55x8.18 [Km2]. As in the previous case, this DEM is represented in projected coordinates (i.e. UTM system).

Figure 12c and Figure 13c show the raw DEM related to the Airport Lake and the Sahara desert. The difference between them is that in the former the points are sampled every 30 meters and in the latter, are sampled every 90 meters. For that reason, the first DEM is denser than the second one.

To calculate the variograms and applying Ordinary Kriging the Matlab mGstat toolbox has been employed. Additionally, the SRTM DEM was first processed in ArcGIS suite (Esri) before using it in Matlab (spherical coordinates to UTM). The stratified sampling approach has been implemented taking advantage of the VL-Feat toolbox. The D* algorithm has been implemented using the Robotics toolbox.

2.3.2. Subsampling Algorithms

In this section, the performance of the subsampling approaches before attempting Kriging and the mobility prediction analysis is examined. In particular, the following sampling approaches are compared: systematic sampling, stratified sampling, and the method based on combining systematic and stratified approaches. These methods have been applied to the Airport Lake and the Sahara desert regions.

It bears mentioning that the tuning parameter (i.e. the number of points or strata) of each subsampling approach has been selected in order to maximize the following metrics: minimum

number of samples, minimum computation time, minimum error in range and sill, maximum correlation with the variogram model (Pearson's correlation coefficient), and maximum correlation with the elevation profile (Pearson's correlation coefficient).

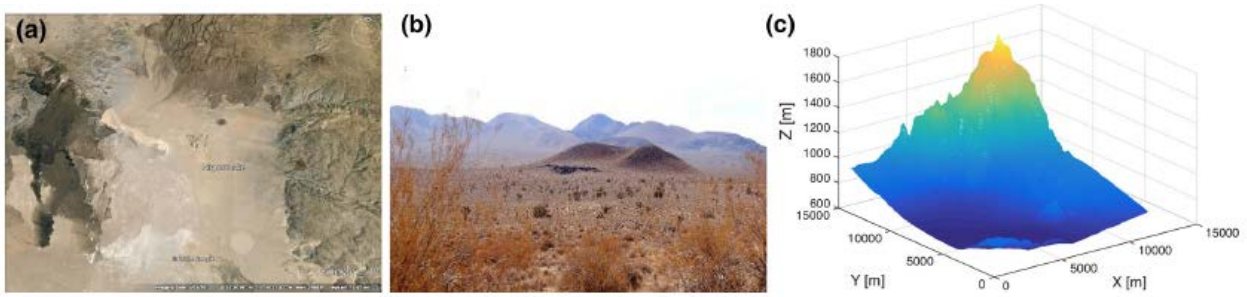

Figure 12. Airport Lake, Death Valley (CA, USA). USGS DEM (30-m resolution)

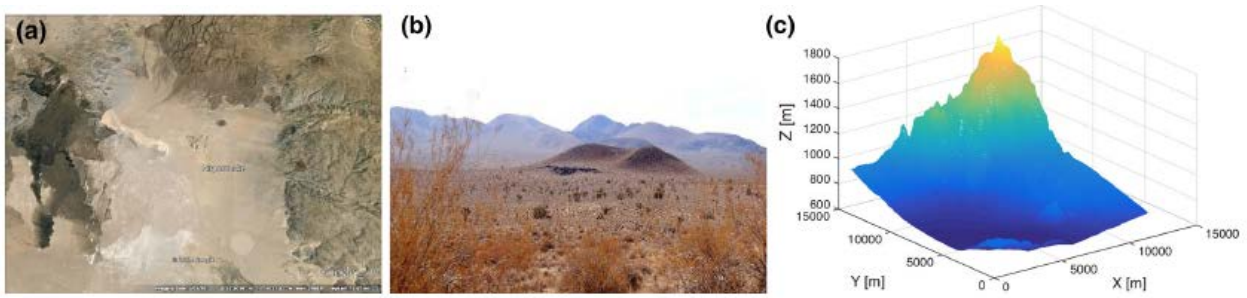

Figure 13. Sahara desert (Chad, Africa). SRTM DEM (90-m resolution)

2.3.2.1. Experiment 1. Airport Lake (Death Valley, CA, USA)

This section details the performance of the subsampling approaches considering the Airport Lake. The stratified sampling has been configured with 300 strata and one random sample has been selected within each strata (K-Means = 300). The systematic approach has been configured in order to obtain a random sample every 90 meters leading to 127 samples. Additionally, two configurations of the proposed method are tested. The first one considered 15 strata and two random points for each strata plus 127 samples from the systematic sampling (156 points, 1 point was filtered). The second configuration deals with 15 strata and one random sample per strata plus 127 samples from the systematic sampling (142 points).

Firstly, we estimate the theoretical variogram of the entire DEM. In this case, the raw DEM is composed of 34741 samples leading to a computation time of 44 minutes (Intel Core i7 3GHz, 16 MB RAM). This variogram is automatically fitted, through the least squares method, by a Gaussian model (5th-order polynomial).

Figures 14a, 14b show the first experiments carried out in order to check the performance of the systematic sampling approach (127 samples, 0.1 seconds) and the stratified sampling approach (300 samples, 0.2 seconds), respectively. The empirical variograms do not fit the Gaussian model that represents the entire DEM (black curve). An interesting conclusion from these experiments is that the stratified sampling approach fits the range of the Gaussian model (5167 versus 5273), but not the sill (81164 versus 29814). In contrast, the systematic sampling method

has a smaller error in the sill (21371 versus 29814), but there is a deviation in the range (4841 versus 5273). Notice that the units of the sill and range are [m^4] and [m], respectively.

Figures 14c, 14d displays the result obtained with the proposed subsampling approach (156 and 142 samples). Observe that the empirical variograms fit better the variogram model obtained with the entire DEM. Especial mention is for the case where two random samples are selected within each strata (Figure 14c). Here, as the range as the sill fit the theoretical variogram model (5089 versus 5273; 28529 versus 29814).

As shown in Figure 15, the points selected by the proposed approach fit properly the elevation profile. Even though, in this regard the best result is obtained using the stratified sampling method.

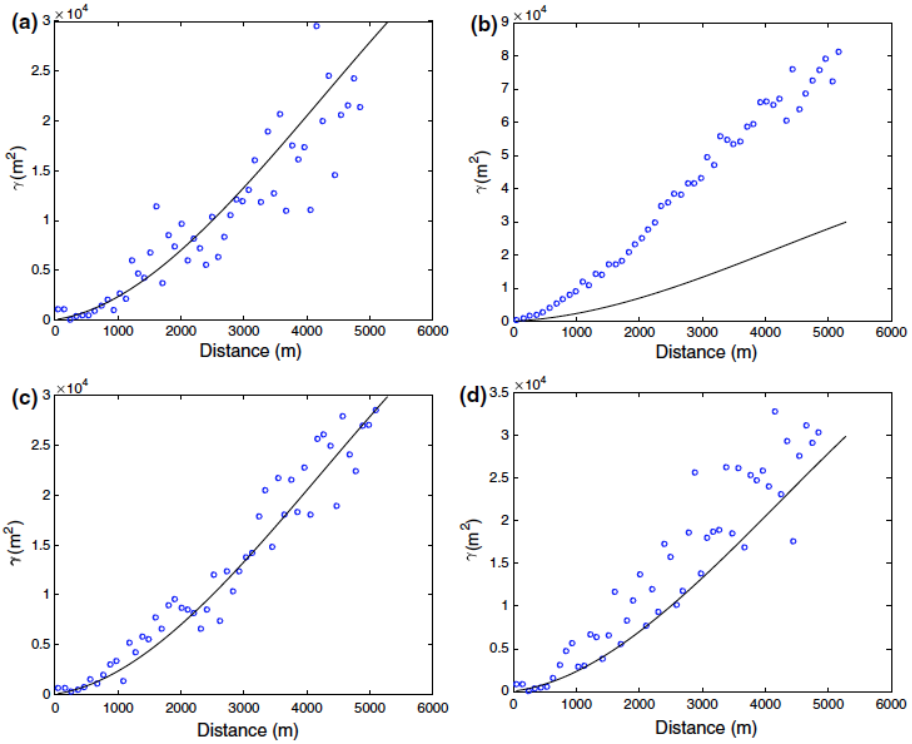

Figure 14. Variograms (Airport Lake). The continuous line is the theoretical variogram considering all the raw samples, the blue circles mean the empirical variogram of each method

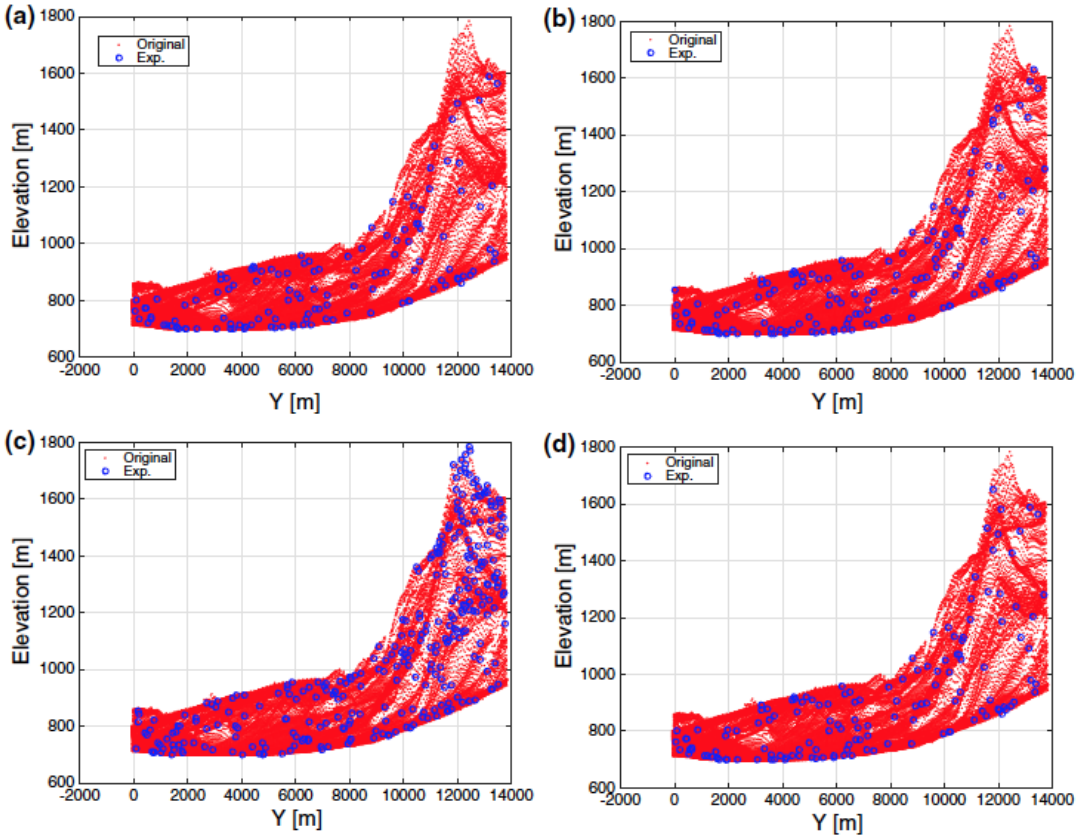

Figure 15. Elevations (Airport Lake). Notice that the circles represent the subsampled points and the red profile the entire data set (raw samples)

2.3.2.2. Experiment 2. Sahara Desert (Chad, Africa)

This section focuses on the performance of the subsampling approaches considering the Sahara desert. The stratified sampling has been experimentally configured with 65 strata and three random samples per strata leading to 195 samples. The systematic approach has been configured in order to obtain 73 samples. The two configurations of the proposed subsampling approach are: 23 strata with one random point for each strata plus 73 samples from the systematic sampling. The second configuration is 23 strata with two random samples per strata plus 73 samples from the systematic sampling.

As in the previous experiments, the theoretical variogram of the entire DEM is first calculated. In this case, the raw DEM is composed of 6660 samples leading to a computation time of 1 minute and 20 seconds (Intel Core i7 3GHz, 16 MB RAM). Figures 16a, 16b show the experiments carried out with the systematic sampling and the stratified sampling approach, respectively. The main result is that the empirical variograms do not fit the Gaussian model that represents the entire DEM. A similar behavior to the previous scenario is observed, that is, the stratified sampling approach fits the range of the Gaussian model (5167 versus 5273), but not the sill (81164 versus 29814). In contrast, the systematic sampling has a smaller error in the sill (21371 versus 29814), but there is a deviation in the range (4841 versus 5273).

Figures 16c, 16d display the result obtained with the proposed subsampling approach (156 and 142 samples). Observe that the empirical variograms fit the variogram model obtained with the entire DEM. The best case is obtained when two random samples are selected within each strata (Figure 15c). Here, as the range as the sill are similar to the theoretical variogram model (5089 versus 5273; 28529 versus 29814). As in the previous experiment, the proposed approach achieves a proper performance fitting the elevation profile, see Figure 17.

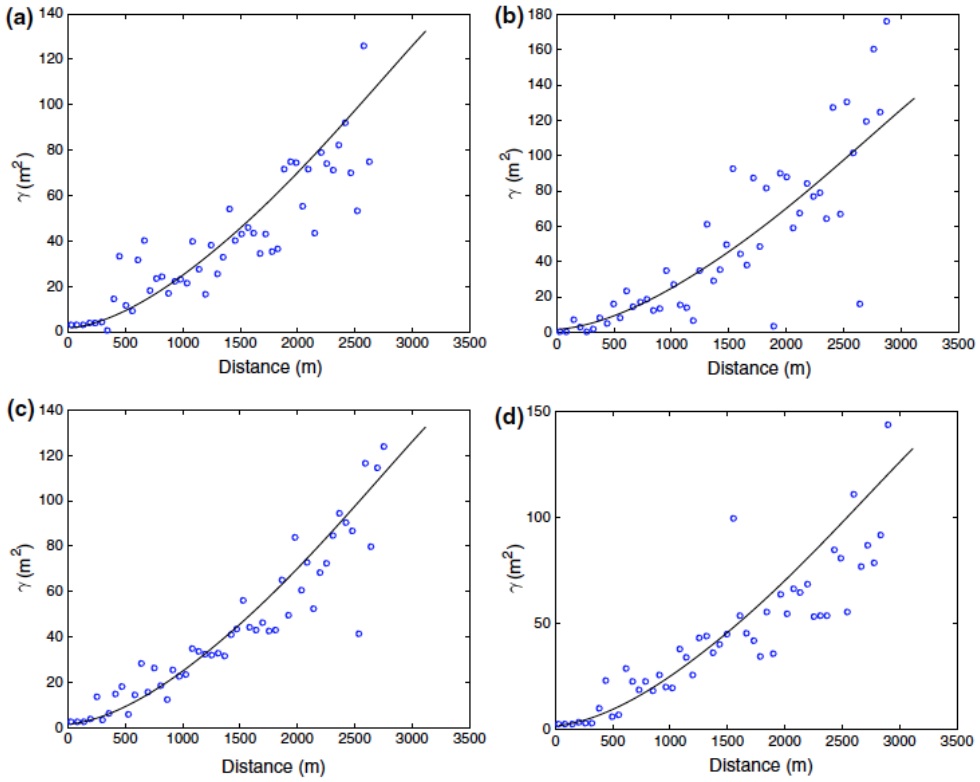

Figure 16. Variograms (Sahara desert). The continuous line is the theoretical variogram considering all the raw samples, the blue circles mean the empirical variogram of each method

2.3.2.3. Discussion about the Subsampling Experiments

In this section, we analyze the results obtained with the subsampling approaches in terms of the following metrics: number of samples, computation time, range and sill of the variograms, Pearson's correlation coefficient between the original variogram and the variogram obtained for each sampling approach, Pearson's correlation coefficient between each elevation profile, and the mean of the squared residuals between the experimental values and the fitted variogram model. In order to calculate the Pearson's correlation coefficients a 5th-order polynomial has been fitted to the empirical variogram and to the elevation profile in each case. Recall that those experiments were run in a COTS computer (Intel Core i7 3GHz, 16 MB RAM).

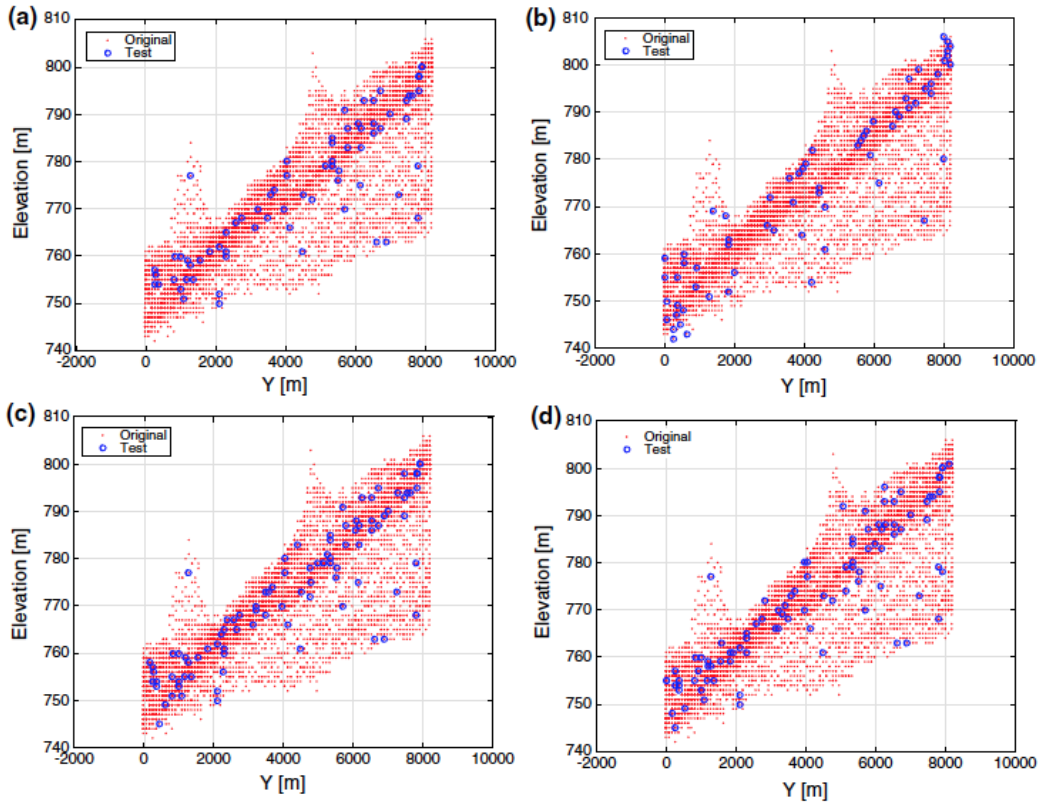

Figure 17. Elevations (Sahara desert). Notice that the circles represent the subsampled points and the red profile the entire data set (raw samples)

Table 1 shows that the subsampling proposed methodology is worthy in terms of computation time and without reducing the precision of the empirical variogram. Notice that the best result is obtained with the two configurations highlighted in the table (156 samples for the Airport Lake and 96 samples for the Sahara Desert). The deviation from the original DEM is the smallest one considering all the metrics. It bears mentioning that the maximum similarity in the elevation profile is usually achieved by the stratified sampling approach. However, this approach yields a poor correlation in terms of the variogram (Pearson's correlation coefficient). This research also draws the following points:

- The number of samples is not directly related to the confidence of the empirical variogram. We demonstrate that 156 samples (Airport Lake) and 96 samples (Sahara Desert) are better than 300 samples and 195 samples, respectively (combined subsampling approach versus stratified subsampling).
- Regarding the sampling step, it is important to take into account not only the elevation of the samples (stratified sampling), but also the distance between points (systematic sampling). The solution that leads to the best metrics is in fact a combination of both approaches (Pearson's correlation coefficient).
- The computation time can be dramatically reduced by selecting the appropriate samples, instead of considering the entire DEM (44 minutes versus 0.1 seconds, in case of the Airport Lake environment).
- The suitability of the combined sampling approach is demonstrated in terms of the range and sill of the variogram and the elevation profile.

It is important to remark that a slight variation in the shape of the variogram (small deviation in the range or sill) has no effect on the ordinary kriging weights and the kriging estimates (elevations). It only affects the kriging variance. For that reason, considering the reduced-order datasets will not affect the kriging performance.

Table 1 Summary of the performance of the subsampling approaches

	No. points	Comp. time	Range (m)	Sill (m^4)	ρ (variogram)	ρ (elev. profile)	Mean residual (m^4)
Airport Lake							
Original DEM	34,741	44 min	5273	29,814	–	–	8.5e3
Systematic sampling	127	0.1 s	4840	21,370	0.9988	0.9809	1.13e7
Stratified sampling	300	0.2 s	5167	81164	0.9916	0.9984	9.41e8
Combined sampling (2 points/strata)	156	0.1 s	5089	28529	0.9991	0.9862	4.73e6
Combined sampling (1 point/strata)	142	0.1 s.	4841	30332	0.9927	0.9882	2.22e7
Sahara desert							
Original DEM	6660	1 min 20 s	3112	132	–	–	1.97e−1
Systematic sampling	73	0.1 s	2626	75	0.9942	0.9868	2.14e4
Stratified sampling	195	0.1 s	2876	176	0.9757	0.9887	5.70e2
Combined sampling (1 point/strata)	96	0.1 s	2756	124	0.9942	0.9862	1.54e2
Combined sampling (2 points/strata)	117	0.1 s.	2897	143	0.9738	0.9944	3.16e5

2.3.3. Ordinary Kriging and Global Path Planning

Once a set of samples have been selected representing the raw DEM, the next step deals with applying the ordinary kriging algorithm in order to obtain a new model of the terrain at a finer resolution. In this case, 10-m resolution models are desired, which leads to an affordable computation burden. After that, the D* algorithm is applied in order to obtain the optimal route between two desired points. Recall that three cost functions are evaluated: min-distance (the shortest route), min-uncertainty (the route with the minimum uncertainty), and min-slope (the flattest route).

Figure 18a details the result of applying ordinary kriging to the Airport Lake environment, and Figure 18b deals with the Sahara Desert. Notice that the generated models fit properly the original DEMs. Furthermore, it is important to highlight the small standard deviation (uncertainty) obtained. In both environments, it is smaller than 0.2 [m] (blue color). Brighter colors mean larger uncertainty, notice that they appear near the boundaries of the surfaces because no samples are available for those regions (from the subsampling step). The range in the standard deviation associated to the Death Valley model is (0, 15.67) [m], the mean value is 0.2 [m] with standard deviation 0.81 [m]. For the Sahara scenario, the range is (0, 4.48) [m], the mean value is 0.05 [m] with standard deviation 0.18 [m].

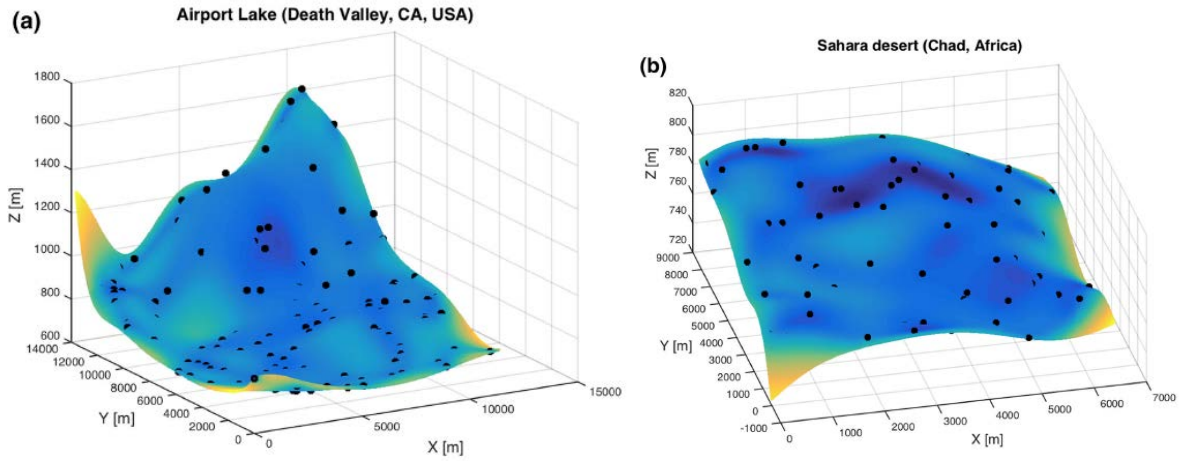

Figure 18. Surface reconstruction using ordinary kriging (stochastic model of the terrain). The original resolutions were 30-m and 90-m, respectively. The new digital elevation models have a resolution of 10 meters. Notice that blue color means low uncertainty, < 0.2 [m] for Death Valley and < 0.05 [m] for Sahara Desert

After obtaining the new models of the terrain with kriging, the D* path planning algorithm is used to obtain the optimal route according to a cost function. Figure 19 shows the min-distance and the min-uncertainty routes for the Airport Lake. As expected, the shortest route (straight-line) corresponds to the min-distance line (red line). The min-uncertainty route considers the variance of the elevation (uncertainty obtained from kriging). For that reason, this route passes as close as possible to the original sampled points (black dots).

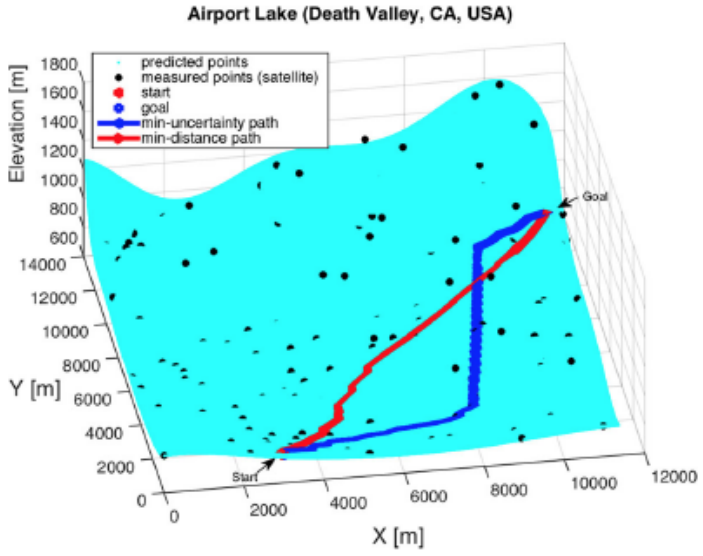

Figure 19. Routes obtained using the D path planner. Notice that the min-uncertainty path goes closer to the actual sampled points. In contrast, the min-distance path follows a straight line between the starting point and the goal. The mesh represents the interpolated model considering the nominal elevations (kriging estimations)*

Figure 20 displays a deterministic terrain profile illustrating the minimum slope between points (8-neighbors to each point). In this sense, a path going through a brighter region (yellow) would mean a flatter route (small variation in the elevation between one point and its neighbor). On the other hand, hazards such as high slopes are represented by blue or red color, that is, the difference in elevation between one point and its neighbors is larger than in a brighter region. Notice that positive values (red color) mean positive slopes (the vehicle would pitch up), and negative values (blue color) represent negative slopes (the vehicle would pitch down).

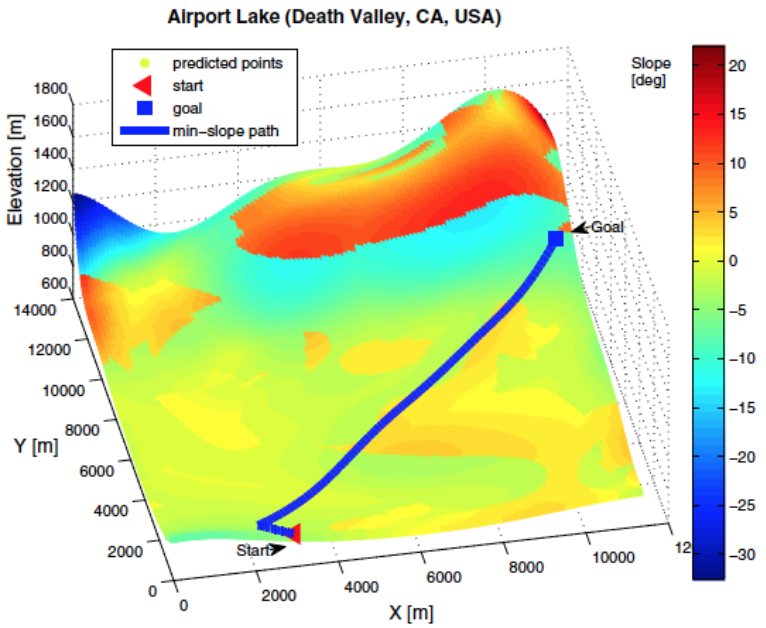

Figure 20. Deterministic terrain profile: representation of the 3D map in terms of the maximum slope between the 8-neighbors around each point and D optimal path minimizing the slope between points. Notice that in order to estimate this map the nominal value of the elevation of each point has been considered*

Figure 21 shows the three routes obtained with the D* algorithm in the x-y plane. Observing these plots is even easier to understand the difference between the three cost functions. For example, the min-distance route follows a straight line between the starting and the goal points, which is expected. However, the min-uncertainty route follows a different pattern. Although a longer path is generated, the ground vehicle would move over a safer route where more “certain points” are traversed (black points). The min-slope route also takes a different path.

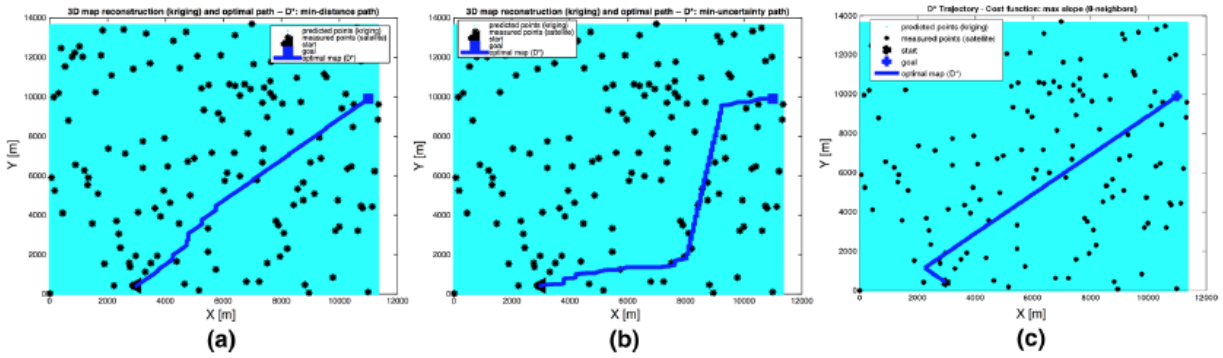

Figure 21. Airport Lake (USA)}. Comparison of the three routes obtained the D algorithm considering the variance (uncertainty) of each point as the cost function (min-uncertainty path), considering the elevation (min-distance path), or the terrain profile (min-slope path)*

Figure 22 shows the min-distance and the min-uncertainty routes regarding the Sahara Desert scenario. Again, the shortest route (straight-line) corresponds to the min-distance line. As expected, the min-uncertainty route passes fairly close to the sampled points, although it means a longer path.

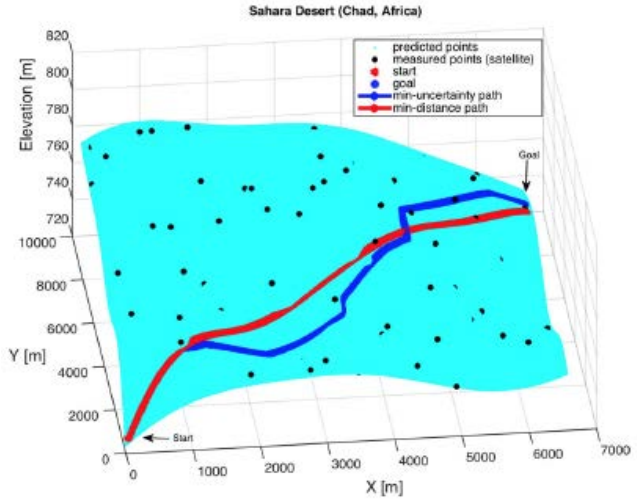

Figure 22. Routes obtained using the D path planner. The mesh represents the interpolated model considering the nominal elevations (kriging estimations)*

Figure 23 displays the deterministic terrain profile dealing with the minimum slope between points. Notice that compared to the previous scenario the Sahara Desert is a flatter scenario, the elevation range is smaller than 100 meters. For that reason, the slope angles are smaller than in the previous environment (range 2.5 to -1.5 [deg]). This fact explains why the min-slope route is quite similar to the min-distance route.

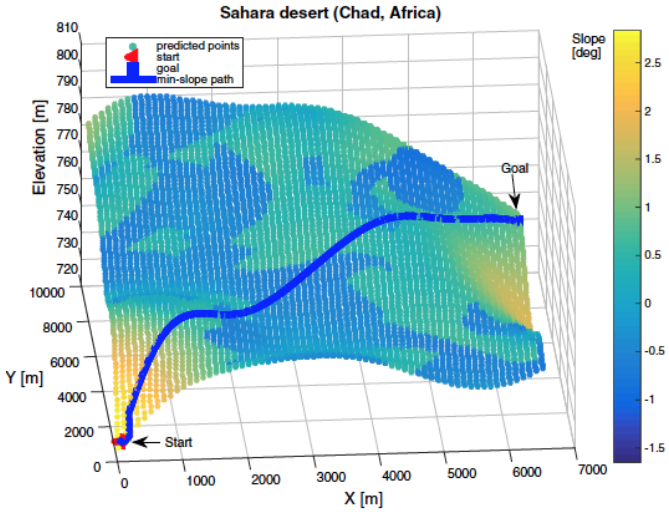

Figure 23. Deterministic terrain profile: representation of the 3D map in terms of the maximum slope between the 8-neighbors around each point and D optimal path minimizing the slope between points*

Finally, Figure 24 shows the three routes obtained with the D* algorithm in the x-y plane. Notice the similarity between the min-distance and the min-slope routes. The main difference still takes place with the min-uncertainty route. As in the previous scenario, a longer path is generated, but with the benefit of following a safer route (smallest uncertainty regarding the true elevation of the terrain).

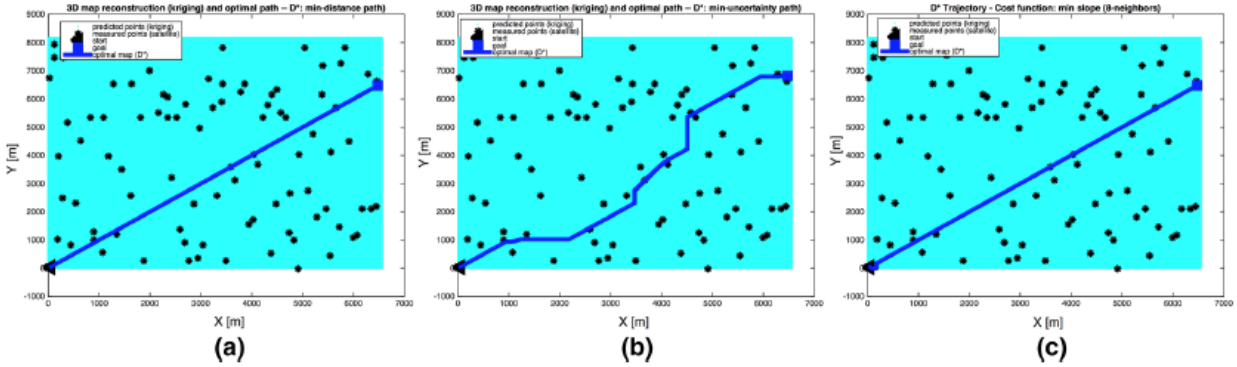

Figure 24. Sahara Desert (Chad)}. Comparison of the three routes obtained the D algorithm considering the variance (uncertainty) of each point as the cost function (min-uncertainty path), considering the elevation (min-distance path), or the terrain profile (min-slope path)*

2.3.4. Mobility Prediction

This section deals with analyzing the mobility of a vehicle over the routes discussed in the previous section. Notice that a maximum linear velocity of 1 [m/s] and a maximum steering angle of 75 [deg] have been assumed for the testbed considering in these experiments. The lookahead distance of the pure pursuit algorithm is 4 [m], and the sampling period is 1 [s]. More technical data about the vehicle configuration is summarized in Table 2. Furthermore, the vehicle is equipped with two Mason DC motors, model 253298 (one motor for traction and another motor for steering).

Table 2 Features of the vehicle considered in this research

Feature	Value
Wheel radius (m)	0.25
Wheelbase (m)	2.5
Terminal resistance (Ω)	0.568
Torque constant (mNm/A)	158
Speed constant (rpm/V)	60.4
Speed/Torque gradient (rpm/mNm)	0.217
Rotor inertia ($g\,cm^2$)	1320

It bears mentioning that 150 Monte Carlo simulations have been carried out for each reference route and for each scenario. It means that a random value for the elevation of each reference point has been generated according to the mean value of the elevation and the Kriging variance.

Table 3 summarizes the performance of each route in terms of the cost functions previously introduced. As expected, the shortest route is obtained employing the min-distance cost in the D* algorithm. The longest route is obtained using the min-uncertainty cost because it was shown it pursues to follow as much “true” samples as possible.

The route with the lowest uncertainty results from the min-uncertainty cost. Recall that this value has been obtained as the mean value of the Kriging variance. For that reason, there is a clear difference between the values obtained in the first scenario and those obtained for the second environment. Uncertainty is larger in the Sahara Desert because the original DEM had a resolution of 90 meters and the new model has a resolution of 10 meters. In contrast, the resolutions of the two models of the Death Valley region are much more similar, 30 meters versus 10 meters. Those results show the importance of uncertainty in elevation and its relation with the spatial resolution.

The trajectory with the lowest mean value for the elevation is given by the min-slope cost. Again, this cost function is given in terms of the average value of the mean elevation. For that reason, when the deterministic terrain profile related to the maximum slope angles between points is considered by the D* algorithm, it is not surprising that it leads to the flattest route.

One interesting conclusion is drawn from the last two columns. First, notice that the energy spent for the two motors of the vehicle (steering motor and traction motor) is fairly similar regarding the min-distance and the min-slope costs because the length of the trajectories is similar in both cases. Even in the first scenario the energy required for the min-slope route is smaller than the min-distance despite the fact it is slightly longer. This is explained because, according to the current configuration of the vehicle (maximum steering angle, maximum linear velocity, etc.), the min-distance route requires more energy to be followed. On the other hand, it bears mentioning that although the min-slope route achieves the minimum value in terms of the mean elevation it does not ensure the smallest value in the slope column. This is not altogether unexpected because the min-slope route has a larger mean uncertain value than the min-uncertainty route. It means that after 150 runs the average value of the slope is smaller when the uncertainty in elevation is smaller. Recall that the index dealing with elevation is obtained as the

average of the mean elevation for each route (Kriging mean), and the column related to the slope results from simulating the Kriging variance associated to each point during 150 runs.

Table 3 Summary of the three cost functions considered in this research

	Length (m)	Uncertainty (m)	Elevation (m)	Energy (Kw)	Slope (°)
Airport Lake (Death Valley, CA, USA)					
Min-distance	12,794	0.05	830	241	2.46
Min-uncertainty	16,617	0.04	853	306	2.17
Min-slope	13,407	0.05	827	221	2.38
Sahara desert (Chad, Africa)					
Min-distance	9079	0.12	766	172	1.33
Min-uncertainty	10,410	0.10	767	196	1.31
Min-slope	9216	0.19	765	174	1.59

The main conclusion of these experiments is that this research demonstrates from a stochastic point of view that the min-uncertainty route is more appropriate than the min-distance and the min-slope routes if uncertainty in elevation is considered. It means that a minimum value in the slope (5th column in Table 3) would eventually lead to a lower consumption. Recall that the fourth column, called Energy, is only calculated for the x-y plane, it does not then account for all the energy required to traverse the 3D world. This issue is in fact shown through a realistic animation discussed in the following section.

Conclusions and Future Work

This work presents a mobility prediction strategy for manned and unmanned ground vehicles planned to operate over large regions (> 5 x 5 [Km^2]). We demonstrate the suitability of stochastic analysis and geostatistics to the global path planning problem. Specifically, two different environments with different elevation profiles have been tested. The first one deals with a ~13 x13 [Km^2] region; the second environment has dimensions of ~8 x 8 [Km^2]. The reason why those two environments have been selected is because they have two different DEM formats and two different resolutions. The Airport Lake DEM has a USGS format with 30-m resolution. The Sahara Desert has an SRTM format with 90-m resolution, what means points are sparser in the second DEM than in the first one. Notice that 30-m resolution DEMs are only available for the US territory so far, worldwide coverage is only available through the SRTM format and 90-m resolution.

An important contribution of this work is that we have demonstrated the importance of considering uncertainty in elevation in the cost function of the path planning algorithm. It not only leads to a safer route but also it could mean a lower consumption. However, depending on the criteria or objective selected, it might not mean the optimal solution (e.g. when the shortest route is desired).

The computation burden is a major issue working with actual digital elevation models of regions larger than 5 x 5 [Km^2] because large datasets have to be handled (e.g. Airport Lake DEM has almost 35000 samples and the model obtained with kriging has almost 2 million points). For this reason, identifying methods for obtaining a reduced-order representation of that DEM constitutes a key point in this field. In this research, a subsampling approach is proposed. It certainly

reduces computation time in the variogram calculation and in the kriging step without reducing the precision of the geostatistics-related metrics. Due to this contribution, we have been able to perform kriging over a reduced-order representation of the DEMs. When we tried kriging over those scenarios with no subsampling algorithm the computer ran out of RAM memory (Intel Core i7 3GHz, 16 MB RAM).

There is not a clear answer to what is the most appropriate spatial resolution in order to perform a reliable stochastic mobility prediction analysis. It is not known whether any detailed study on this issue has been performed. It appears that spatial resolution of data for 3D terrain models should be dependent on the size of the vehicle, the variability of the terrain, and on the nature of any natural or man-made obstacles that the vehicle must negotiate. In this research, a resolution of 10 meters has been considered for the interpolated model of the terrain (originally such model was 30-m or 90-m resolution) because the length of the intended vehicle (i.e. Humvee military vehicle) has a length of 5 meters. Smaller resolutions to 10 meters led to unfeasible solutions (computer ran out of RAM memory). This key point will be considered in the coming research.

Future efforts will focus on combining uncertainty in elevation with information from the terrain itself (i.e. terrain trafficability). This issue will lead to more reliable and safer routes. Firstly, taking into account uncertainty in elevation will lead to more efficient routes, and secondly, considering terrain information will reduce the risk of vehicle entrapment.

3. An Efficient Method for Increasing the Accuracy of Mobility Maps

3.1. Increasing kriging accuracy through segmentation-based local variograms

The method proposed in this work aims at dividing the terrain profile into simpler segments with homogeneous properties, that is, with a similar fractal dimension or a similar elevation range. Similar fractal dimension also means similar range, sill, and shape of the local variograms, which ultimately results in similar spatial profile. On the other hand, the elevation range is applied when the first metrics cannot be calculated, instead segments are clustered depending on the elevation. In particular, the proposed method concerns the following steps:

- The first step is to divide the environment into small segments. In this regard, the well-known clustering algorithm K-means has been employed. The initial number of segments (or clusters in the K-means algorithm) is provided by the user (see Remark 1).
- The Fractal Dimension (FD) and the Elevation Range (ER) are both obtained for each small segment (local variograms). FD and ER are introduced in the next section.
- Those segments with similar FD or ER are merged (segment growing).

Remark 1 Notice that the initial number of segments (or clusters) are provided by the user. A large value for K may lead to small segments such that there are not enough points to calculate the variogram. In contrast, a small value for K may mean that non-stationarity remains in the identified segments. For that reason, K is incrementally increased until convergence is achieved (i.e. the number of merged segments becomes constant).

3.1.1. Segmentation based on fractal dimension and elevation range

Recall that the goal of land surface segmentation is to distinguish segments that are homogeneous morphologically. To date, the common way to proceed is based on using the FD metrics in order to merge homogeneous segments. In geostatistical terms, this property is fulfilled when the variogram grows from a small value in the semivariance to a higher value as the lag increases. When the surface is almost flat, the assumption of fractional Brownian surface is not valid.

Two common metrics are often used in the field of geomorphology to replace FD when the region is not a Brownian surface: (1) the slope of the variogram and (2) the ER. The slope of the variogram has the disadvantage that the range and sill are not considered; thus, various segments may have the same slope of the variogram but they are actually quite different (e.g. different roughness). ER is employed in this work instead to merge flat segments (standard deviation of ER is smaller than a given threshold). When the segment fulfills Brownian properties, the FD is used instead. This procedure combines the advantages of FD, comprising variogram information into one single number (slope, range, and sill), and the detection of flat surfaces.

3.2. Illustrative examples

3.2.1. Study sites

In order to demonstrate the suitability of the proposed segmentation approach three different segments have been considered. Those segments address heterogeneous surfaces (i.e. composed of non-stationary segments). The first two scenarios are related to natural terrains. The last scenario combines natural segments with man-made segments (urban environment).

It is important to point out that the regions considered are formatted according to the 7.5-Min DEM of the US Geological Survey agency. It means that each DEM has a resolution of 30 meters. The goal is to obtain a new model of the terrain to a higher resolution, in this case, 15 meters.

3.2.2. Segmentation based on fractal dimension and elevation range

Once the study sites are introduced, this section analyzes the performance of the proposed approach against the traditional interpolation based on considering a single variogram for the entire environment (global variogram). Firstly, the convergence of the segmentation-based method is analyzed in terms of the number of clustered segments and the initial number of clusters for the K-means algorithm. After that, the performance of the segmentation-based approach is graphically and quantitatively examined for each study site.

Table 1 shows the number of merged segments after applying the proposed approach to the first scenario (Mojave Desert). Recall that, K-means is initially used to divide the environment into smaller segments (K = 30, 50, 60, 79, 80, 90); this result therefore demonstrates that the segmentation algorithm converges to 7 segments for values higher than 50. It indicates that the total number of merged segments is 7, no matter the initial number of clusters tuned for K-means. In order to avoid the random effect of K-means when generating the original segments, the same experiment has been repeated five times. Notice that the tuning parameters for the

proposed method are the range in the fractal dimension metrics (denoted as Delta_FD in the table), and the standard deviation in the elevation (denoted as std(ER)). In this case, Delta_FD = 0.2 means that segments within a distance of 0.2 in the fractal dimension metrics are grouped together. When FD cannot be applied, those segments with a standard deviation in the elevation less than 0.5 meters are merged. It bears mentioning that the maximum number of clusters for K-means has been 90 because a larger value leads to a number of samples so small that the variogram model cannot be accurately fitted. This issue depends on the dimensions of the environment considered, for that reason, the maximum number of centers for K-means changes at each experiment.
Table 2 shows the number of merged segments in the second scenario (Death Valley). These results converge to a value of 8 segments whatever the value of K from 19 to 40.

Table 1
Performance of the segmentation-based approach for the Tecopa region (Brownian-like environment).

K	30	50	60	70	80	90
$\Delta_{FD} = 0.2$, $std(ER) < 0.5$	{3, 3, 3, 3, 3}	{7, 7, 7, 6, 6}	{6, 7, 6, 6, 7}	{7, 6, 7, 6, 6}	{7, 7, 7, 6, 7}	{7, 7, 6, 7, 6}

Table 2
Performance of the segmentation-based approach for the Airport lake (flat and rough segments).

K	5	10	15	17	19	20	30	40
$\Delta_{FD} = 0.2$, $std(ER) < 0.5$	{4, 4, 4, 4, 4}	{5, 4, 5, 4, 5}	{4, 5, 5, 6, 5}	{7, 7, 5, 6, 7}	{8, 7, 8, 8, 7}	{8, 8, 7, 8, 8}	{8, 7, 8, 7, 8}	{8, 9, 8, 8, 8}

Finally, Table 3 shows the number of merged segments regarding the third scenario (Barnstable). These results converge to a value of 8 segments after 30 centers are considered for K-means.

Table 3
Performance of the segmentation-based approach for the Hyannis village (natural and man-made segments).

K	10	20	30	35
$\Delta_{FD} = 0.2$, $std(ER) < 0.5$	{4, 5, 5, 5, 3}	{8, 7, 7, 7, 7}	{8, 7, 8, 8, 8}	{9, 8, 8, 8, 8}

Figure 25 shows the two metrics used in the proposed method for the first scenario. More specifically, Figure 25a shows the fractal dimension associated with each segment and Figure 25b shows the elevation range (and the standard deviation of each segment). Due to the uneven terrain profile, it is not altogether unexpected to see high values for the fractal dimension. This fact is also related to the high variance observed in Figure 25b for each segment. The fractal dimension metric is plotted in Figure 25c. The best-fitting line produced when the log values of the variogram are considered is displayed. Notice the small residual error in all the cases, the maximum residual error is in segment 9 with R = 1.73 (R is the residual error related to the best-fitting line). This fact was expected because this environment is a Brownian-like surface.

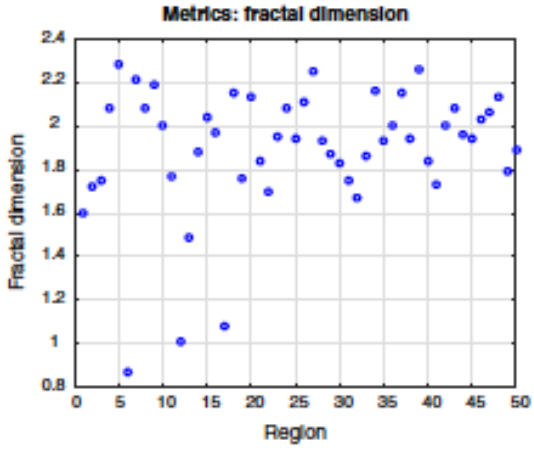

(a) Fractal dimension

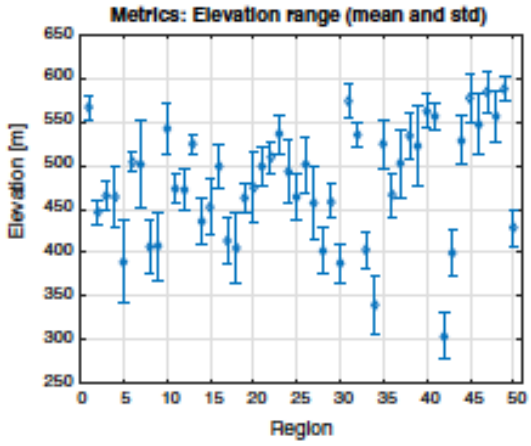

(b) Elevation range (mean and std)

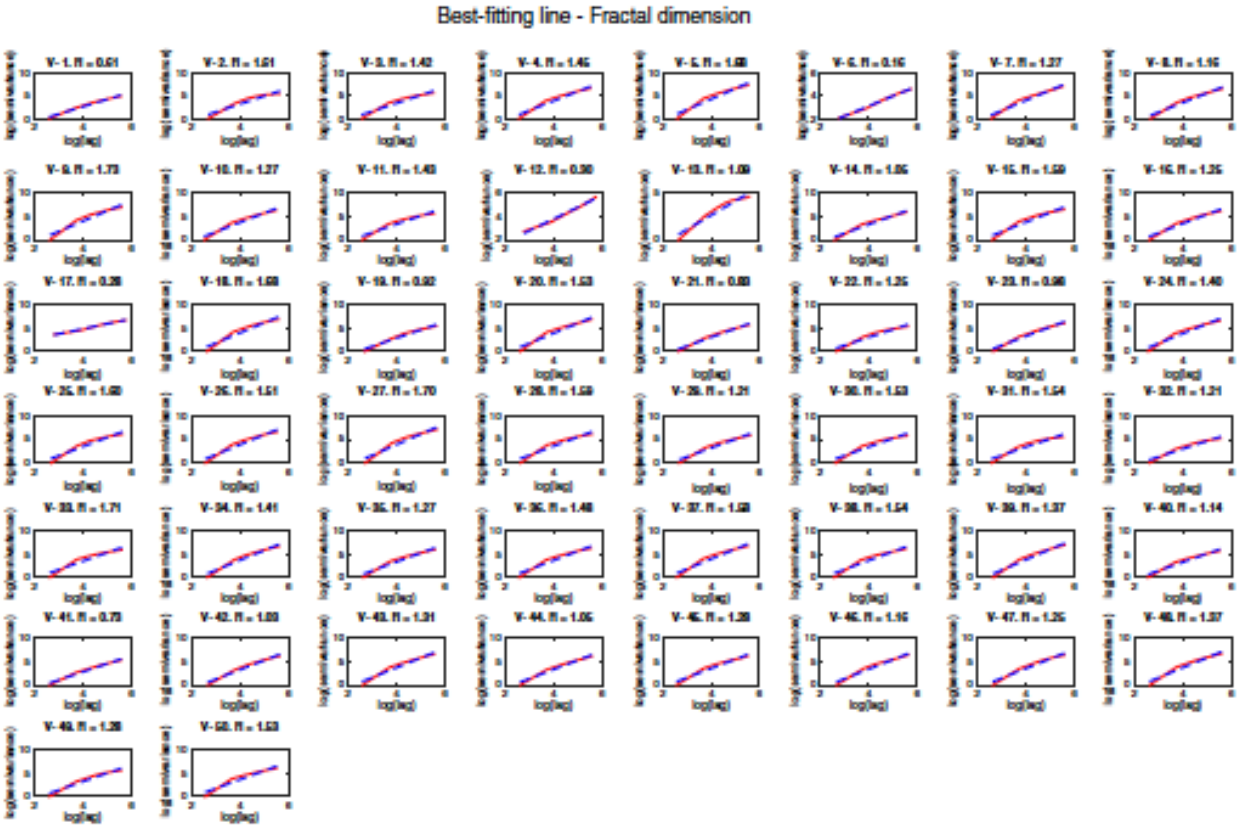

(c) Best-fitting line used for estimating the fractal dimension metrics

Figure 25. Metrics used for the merging the segments. Tecopa region (Brownian-like environment)

Figure 26 shows the fractal dimension and elevation range for the second environment. In contrast to the previous scenario, there are four flat segments where the fractal dimension metrics cannot be applied (i.e. the residual error related to the best-fitting line is larger than 1). This fact

is actually observed in Figure 26c where segments: 3, 6, 10 and 11 have a residual error of R = 3.20, 1.68, 3.14, 1.78), respectively.

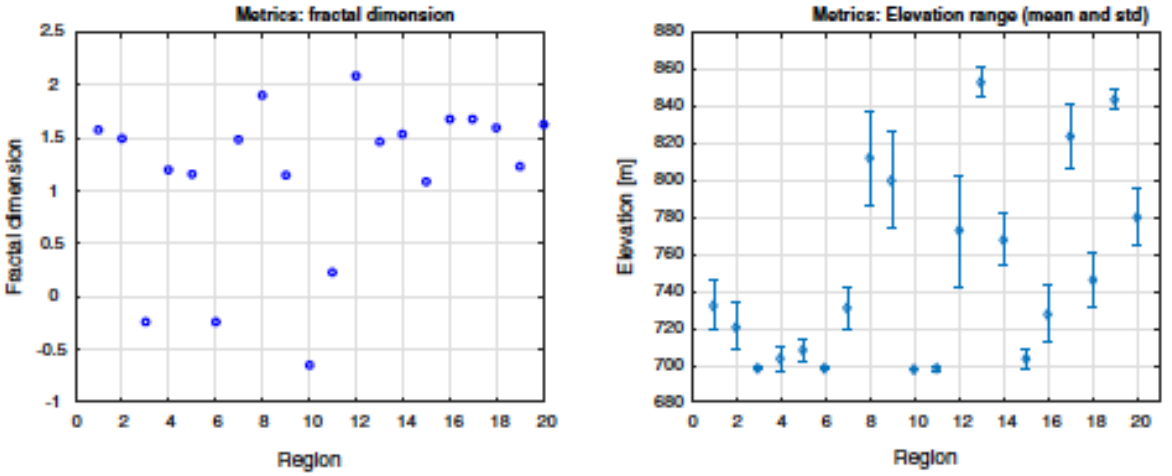

(a) Fractal dimension (b) Elevation range (mean and std)

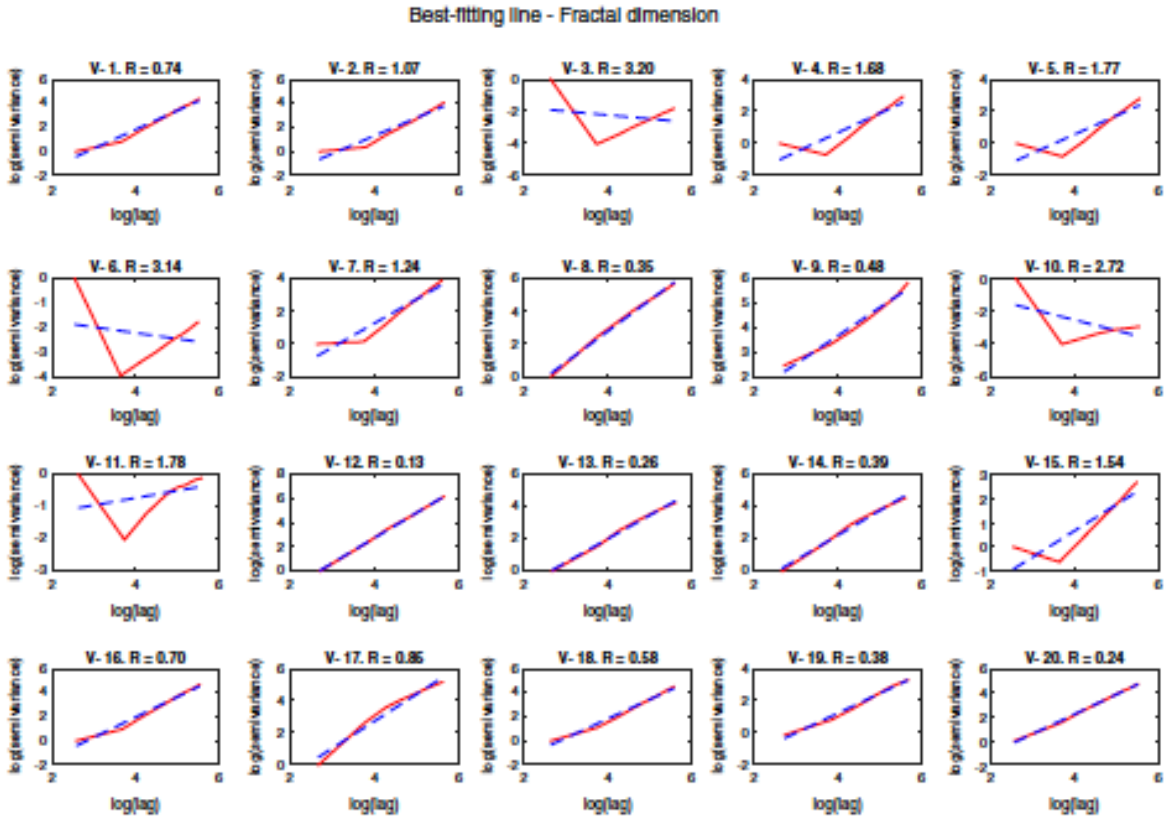

(c) Best-fitting line used for estimating the fractal dimension metrics

Figure 26. Metrics used for merging the segments. Airport lake (flat and rough segments)

Figure 27 shows the fractal dimension and elevation range for the last scenario. There are four flat segments where the fractal dimension metrics cannot be applied for grouping the segments. Notice the small FD values of the segment 9. As observed in Figure 27c, the FD index cannot be

calculated for segments 17, 23, and 25, because they are completely flat segments. This fact is also explained in Figure 27b, where those segments have a standard deviation of zero.

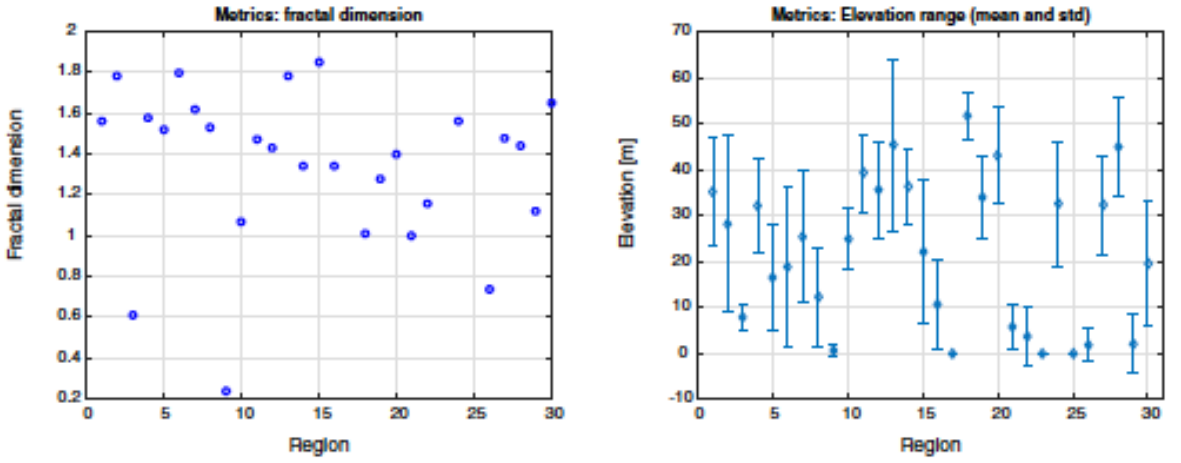

(a) Fractal dimension (b) Elevation range (mean and std)

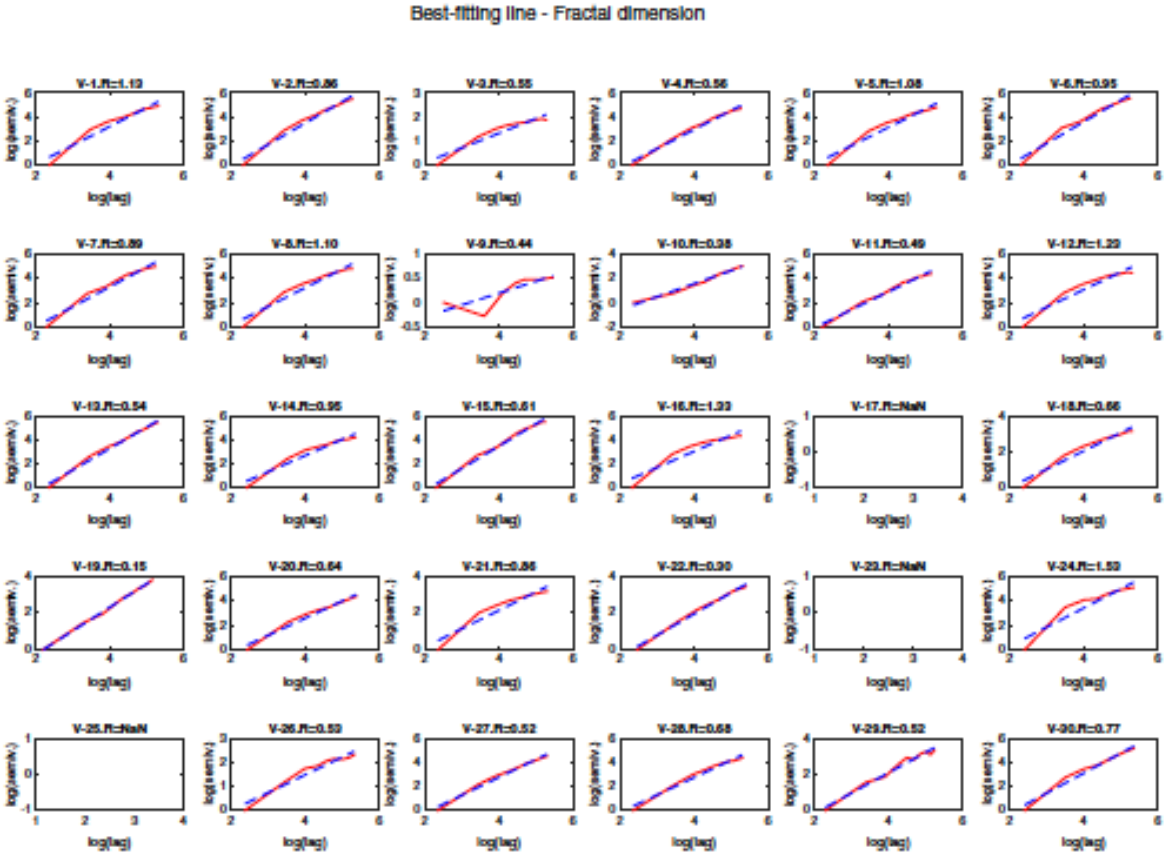

(c) Best-fitting line used for estimating the fractal dimension metrics

Fig. 9. Metrics used for merging the segments. Hyannis village (natural and man-made segments).

Figure 27 Metrics used for merging the segments. Hyannis village (natural and man-made segments)

These last two examples demonstrate the performance of the segmentation algorithm proposed in this work. Additionally, it validates the suitability and generality of the second metrics considered in this work, in addition to the fractal dimension alone.

3.2.3. Kriging interpolation and computation time

This section discusses both the accuracy achieved when the proposed method is employed with kriging in comparison with the traditional way to proceed (global variogram). Computation time of both approaches is analyzed as well. Recall that simulations have been run on a standard-performance computer (Intel Core i7, 3GHz, 16 MB RAM).

Tables 4-6 show that local variograms lead to small kriging variance or error than the traditional approach based on the global variogram (one single variogram for the whole scenario). In this case, the proposed segmentation-based algorithm found 10, 6, and 6 segments for the three scenarios addressed previously (see labels Si in the tables).

Table 4 addresses the first scenario (Mojave Desert). This table demonstrates the two main goals of this paper, that is, smaller kriging error or variance and smaller computation time than when the global variogram is used. In this case, all the segments have a smaller kriging variance than the global variogram except for segments S3 and S6. This result is not altogether unexpected because certain local variograms may lead to over-sampling or under-sampling the new surface. Another significant contribution of this work lies in the computation time. In this case, the computation time related to the proposed segmentation method is slightly higher than 2 minutes and 30 seconds. However, the computation time required by the traditional approach, considering the global variogram, is higher than 1 hour and 36 minutes.

Table 5 shows the results regarding the second scenario. It is important to point out that the mean value and the standard deviation of the kriging variance is smaller than considering the global variogram in all the cases except in the segment L4. Some hypotheses of this fact are: high value in the sill may lead to over-sampling or under-sampling the new surface, and the second possibility is that segment $S4$ is too steep that it does not fulfill the Brownian assumption. As in the previous case, this result also demonstrates the efficiency of the proposed method. Notice that the total computation time required to perform kriging using the local variograms is smaller than 2 minutes. However, performing kriging for the entire environment using the global variogram leads to more than 1 hour and 36 minutes.

Finally, Table 6 shows the results regarding the third environment. In all but two cases (segments S4 and S5), the mean value and the standard deviation of the kriging variance is smaller than considering the global variogram. The total computation time required to perform kriging using the local variograms is smaller than 2 minutes. However, performing kriging for the entire environment using the global variogram leads to more than 1 hour.

Table 4
Statistics related to the kriging variance. Tecopa region (Mojave desert, CA, USA).

Segment	Max (m)	Mean (m)	Std (m)	Times (s)
Global	18.18	12.18	7.33	5766
S1	5.16	3.44	2.09	18
S2	18.47	12.11	7.59	3
S3	39.06	26.05	15.84	14
S4	5.90	3.93	2.40	9
S5	13.10	8.71	5.32	10
S6	22.16	14.78	8.98	14
S7	10.55	7.05	4.27	30
S8	10.23	6.80	4.16	11
S9	5.73	3.83	2.32	25
S10	11.35	7.57	4.60	16

Table 5
Statistics related to the kriging variance. Airport lake (Death valley, CA, USA).

Segment	Max (m)	Mean (m)	Std (m)	Times (s)
Global	40.55	9.33	5.80	5811
S1	5.68	1.43	0.95	25
S2	31.13	4.65	3.87	22
S3	19.43	4.68	3.01	24
S4	51.91	12.47	7.98	20
S5	29.66	7.12	4.54	18
S6	17.32	2.69	1.89	22

Table 6
Statistics related to the kriging variance. Hyannis (Barnstable, MA, USA).

Segment	Max (m)	Mean (m)	Std (m)	Times (s)
Global	28.15	6.44	3.95	3894
S1	0.69	0.46	0.28	19
S2	9.86	3.38	2.05	13
S3	4.75	3.18	1.92	18
S4	39.10	11.91	7.45	7
S5	16.42	11.01	6.63	19
S6	2.14	1.43	0.86	21

3.3. Conclusions

The work shows the suitability of combining two metrics, fractal dimension and elevation range, for increasing the accuracy associated with the known interpolation method kriging. This result leads to more accurate mobility maps when such maps require of an interpolation method in order to increase the resolution. In this context, the proposed method means a significant contribution since previous approaches only deal with Brownian-like surfaces (natural

environments). More specifically, the proposed method ensures non-stationarity both in natural (i.e. Brownian-like) environments and in man-made environments or a combination of them.

Results indicate that the proposed method is more accurate than the global variogram. This contribution is validated considering three different scenarios: the kriging variance or uncertainty associated with those new points is smaller than when the global variogram is considered.

Another important contribution lies in an efficient computation. Efficiency is understood in terms of being able to run the proposed methodology on a standard-performance computer in a reasonable computation time (Intel Core i7, 3GHz, 16 MB RAM). In particular, the computation time of the suggested approach is approximately 2 minutes and applying the traditional approach leads to 1 hour for the same scenario.

The proposed method might be employed for any kind of application that requires ordinary kriging. In this sense, future work will address the practical application of the method suggested in this work (e.g. validating the results obtained here with accurate GPS measurements).

4. Thermal vision, moisture content, and vegetation in traversability prediction

4.1. Modeling thermal inertia

Thermal inertia is a measure of the resistance of a material to changes in temperature. In the context of this work, this thermal property is a function of: grain size, cementation (i.e. cohesion), and porosity (i.e. volume of voids) of a soil. For those reasons, thermal inertia has a major impact on the compaction, and the penetration resistance of a soil. Thermal inertia is defined as $I = sqrt(\rho\, k\, c)$, where ρ is the bulk density, k is the thermal conductivity, and c is the specific heat of the material. Thermal inertia cannot be calculated directly and retrieving it is far from trivial. Here, the Apparent Thermal Inertia (ATI) is calculated $I = (1\text{-}A)/ (T_{day} - T_{night})$, where A is the surface albedo. Among others, this model may lead to inaccurate results when intermountain and highly irrigated regions are considered.

The use of ATI sacrifices accuracy in favor of an explicit simple formula having a straightforward physical interpretation. It bears mentioning that the solution based on the heat transfer model is not free of inaccuracies and uncertainties because of the following issues: (1) it requires the knowledge of various parameters that are not measurable and need to be estimated; (2) it requires numerical methods for solving the set of equations; (3) the computational cost is also considerable. For all those reasons, the ATI model is used in this work for estimating thermal inertia. In any case, the values of thermal inertia obtained in this work are quite similar to those values obtained in similar conditions using the more complicated model.

4.2. Experimental setup

Field experiments were performed on a testing site built for this particular occasion. Three main issues were raised during the building process: (1) scalable and modular configuration where various soils can be tested; (2) comfortable arrangement able to manage easily the bulky and heavy soil sacks required to fill the bins; (3) accessible disposition able to place cameras, sensors, and all the computing elements required.

Figure 28 shows the testing site developed by the authors in Almeria (Spain). Four bins with four representative soil types were first assembled. Those containers have dimensions of 1 [m] wide, 1 [m] length, and 0.5 [m] depth. These dimensions were determined after reviewing several studies dealing with terrain characterization. In those studies, the maximum penetration was normally less than 0.5 meters. Soils were cleaned, dried, and sieved, before being stored in the bins. The four soils mean a broad range of soil properties and, hence, different thermal properties are obtained. It is important to point out that no compaction process was applied to the soil bins; thus, compaction is only due to gravity and moisture content (in the wet-sand bin).

A second configuration of the testing site was also under investigation. This configuration is displayed at the top left corner of Figure 28. Here, the wet- and dry-sand bins were replaced by a vegetated soil bin (barley) and a new sand bin. In addition to that, an artificial lighting system was installed to light/heat the surfaces at night. The main features of this lighting system are: power 500 [W], height 1.5 [m], and hours of operation from 12 am to 8:30 am.

Figure 28. Testing site specifically built for these experiments. Notice the modular and scalable configuration of the soil bins as well as the accessible disposition of the place for setting sensors and hardware. Observe, at the top left corner, the second configuration of this testing site with a soil bin with grass (top right corner) and the artificial lighting system used at night

4.2.1. Sensors and hardware

In order to have a general knowledge of the thermal and weather conditions available during the experiments and for validating the temperatures measured by the thermal camera, a broad set of sensors were installed in the testing site. It bears mentioning that all the sensors have been replicated for redundancy and fault tolerance, this explains the broad set of sensors used here (24 sensors). The sampling period for all the sensors was 1 minute. Some of the sensors used can be seen in Figure 28.

As detailed in Table 1, various temperature probes were submerged in each soil bin for measuring the temperature at approximately 0.01 [m] below the surface. Two weather stations measuring atmospheric temperature, relative humidity, and wind speed were placed in opposite sides of the soil bins for redundancy. All the signals generated in this testing site were monitored by means of four data loggers (Campbell Scientific, CR3000), and two laptops (Dell Precision M2300, Intel Core 2 Duo, 2.50 GHz, 4 GB). All the sensors are sold by Campbell Scientific, but the wind sensor was sold by Gill.

Table 1
Main features of the sensors used to monitor thermal and weather conditions in the testing site.

Sensor	Model	Units/place	Features
Temperature probe	T-108	8/2 for each soil bin	Range: −5 to 95 °C, tolerance: ±0.2 °C
Averaging soil thermocouple probe	T-CAV	3/1 for each soil bin (except bedrock)	Range: −270 to 300 °C
Moisture meter	CS616	2/dry and wet sand bins	Range: ±0.7 V square wave, accuracy: ±2.5%, resolution: 0.1%
Pyranometer	SP1110	2/1 for each weather station	Range: 0–1750 W/m^2, accuracy: ±5%
Temperature and relative humidity probe	CS215	2/1 for each weather station	Humidity: range: 0–100%, accuracy: ±2%, resolution: 0.03%; temperature: range: −40 to 70 °C, accuracy: ±0.3°, resolution: 0.01°
Ultrasonic wind sensor	Windsonic	2/1 for each weather station	Range: 0–60 m/s, wind direction: 0–359°, accuracy: ±2% at 12 m/s, resolution: 0.01 m/s

4.2.2. Thermal and visual cameras

The key component of the testing site is the thermal camera. In this case, the compact 1.4-kg infrared camera ThermoVision A40-M of the company FLIR Systems is employed. This thermal camera has a spectral infrared range of 7.5 to 13 μm, a temperature range of -40 to 120 [deg, C]. The detector is a focal plane array, uncooled microbolometer of 320 x 240 pixels and a field of view of 24 x 18 degrees. The thermal sensitivity is of 0.08 degrees at 30 [deg, C]. The image processing software used for operating the camera is ThermaCAM Researcher Pro 2.8 SR-3. In this case, images are taken every minute (period = 1 minute).

In addition to the thermal camera, a visual camera has been placed in the testing site (Logitech QuickCam Sphere). This camera is synchronized with the thermal camera, which allows to understand better the thermal images. The software for recording video with this camera was WebcamXP.

Figure 29 displays the four soil bins during the first configuration of the testing site (tags: bedrock, wet sand, gravel, dry sand) at 3pm, which means the time when the temperature difference is larger. Observe the temperature differences between the soil bins. The element in the middle, tagged as “Silverwork”, was used for calculating the background radiation level.

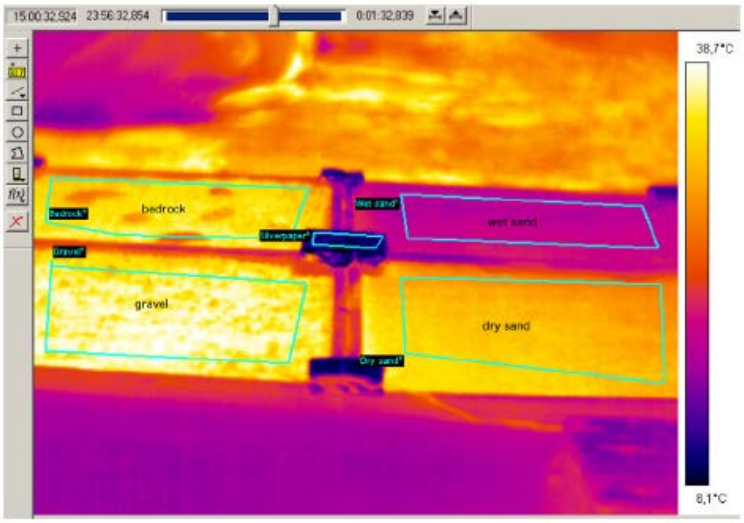

Figure 29. Thermal view of the first configuration of the testing site. Notice that at 3 pm the hottest sample is gravel and the coldest is wet sand

4.3. Terrain characterization

This section addresses the terrain characterization step performed before running the experiments with the thermal camera. Observe that three sets of measurements have been collected in order to properly characterize the soil bins considered in this work. Those experiments were run according to two official European Standards: UNE-EN 933-1:2012 and UNE 103900:2013. The last section addresses a quantitative analysis of terrain traversability.

It bears mentioning that the experiments addressed in the first subsection, sieving method, have been performed in a laboratory (gradation test). The experiments described in the next subsection, nuclear method, were conducted in the testing site, see Figure 30d.

4.3.1. Determination of particle size distribution. Sieving method

The sieving method or gradation test constitutes a common procedure in civil engineering. It describes the engineering properties of a soil based on the size of the particles, the amounts of the various sizes and the characteristics of the very fine grains. The result of the sieving method is provided in terms of a graph of percent passing versus the sieve size, this gives the type of gradation of the soil. This gradation of the soil can be used for classifying the soil. In this case, the Unified Soil Classification System (USCS) has been used for that purpose.

The results obtained are plotted in Figure 30. As observed, gravel and sand represent poor graded soils, that is, they have aggregate of approximately the same size. The curve on the gradation graph is very steep and occupies a small range of the aggregate. In contrast, bedrock constitutes a well graded soil composed of equal amounts of various sizes of aggregate. This explains the even curve on the gradation graph. In gravel, 97% of the samples are retained between the 12.5-mm and 5-mm sieves. This also explains why gravel has very little fine aggregate particles (less than 1% are smaller than 4 [mm]). According to this result, this soil can be classified, following USCS, as: poorly graded gravel (GP). Sand shows a similar result to that previously mentioned, poorly graded soil, but now the samples are trapped in smaller sieves. In particular, 94% of the samples are smaller than 2 [mm]. This soil can be classified as: poorly graded sand (SP). Finally,

bedrock is composed of a wide range of particle sizes and has a good representation of all sizes starting from 10 [mm] to 0.063 [mm]. For that reason, this soil is classified as: well-graded sand (SW).

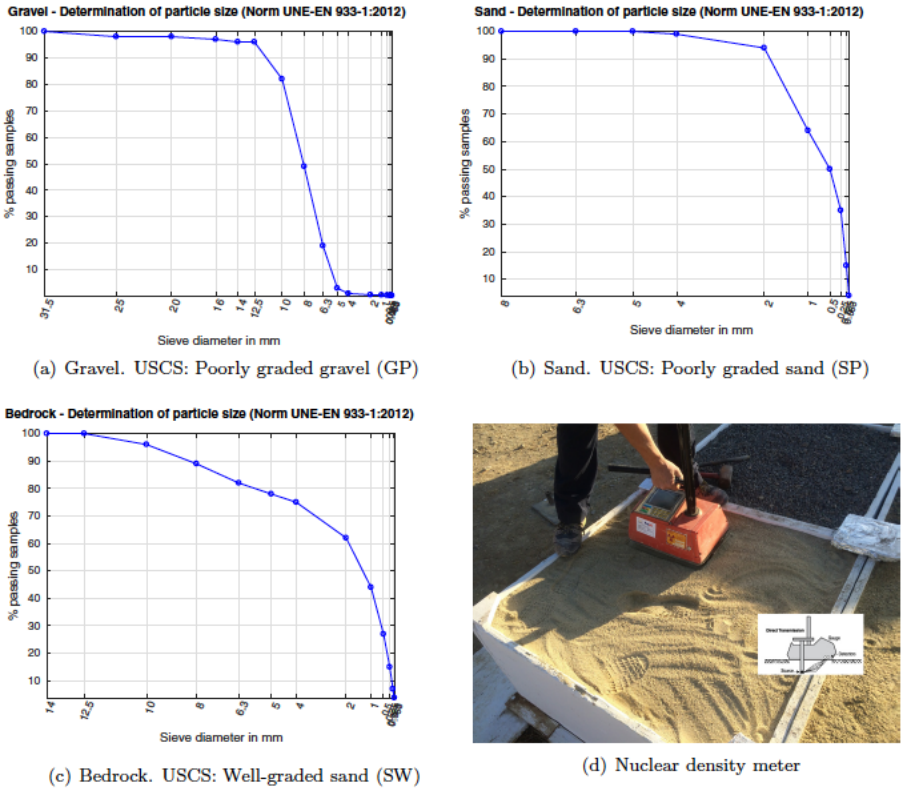

(a) Gravel. USCS: Poorly graded gravel (GP)

(b) Sand. USCS: Poorly graded sand (SP)

(c) Bedrock. USCS: Well-graded sand (SW)

(d) Nuclear density meter

Figure 30. Sieve results after passing the soil samples through the column of sieves. Notice the narrow or uniform gradation of gravel and sand and the dense gradation of bedrock. The nuclear meter is also displayed during operation on the testing site

4.3.2. Determination of density and moisture content. Nuclear methods

With the purpose of determining the density and moisture content that are going to be considered as ground-truth in this work a fairly accurate device has been employed: a nuclear density meter. This device uses a radioactive isotope source that emits photons (usually Gamma rays) which radiate back to the meter's detectors at the bottom of the unit. Dense soil absorbs more radiation than loose soil and the readings reflect overall density.

Table 2 shows the moisture content and density of the six soils measured with the nuclear meter. It bears mentioning that in this case the probe was nailed down at a depth of 0.3 [m] (recall that the depth of the soil bins is 0.5 [m]).

Observe that "dry" sand has a moisture content of 3.96%. This is not altogether unexpected because in nature the air contains water vapor and it is then almost impossible to achieve a moisture content of 0% in sand specially at a depth of 0.3 [m]. In any case, notice that the dry density of dry sand and wet sand is different; this result was expected because in the same volume less particles (less mass) is present in wet sand than in dry sand as the air voids are filled with water. As previously explained, bedrock represents a well-graded soil, it leads to a dense structure because small particles fill the voids in the large particles. This structure explains why bedrock achieves the highest density. In addition to that, bedrock shows a certain moisture

content, 1.68%, because it is partially composed of dry sand. The density of gravel is quite similar to dry sand, this is explained because even though the particles are larger than sand, there are air voids between particles. This increases the volume but reduces the mass.

Table 2
Density and moisture content obtained with the nuclear meter at a depth of 0.3 [m].

Sample	Moisture content (%)	Wet density (kg/m^3)	Dry density (kg/m^3)
Dry sand	3.96	1.66	1.59
Wet sand	19.10	1.58	1.32
Sand	12.01	1.60	1.45
Bedrock	1.68	1.87	1.84
Gravel	0.23	1.60	1.59
Grass	6.01	1.64	1.55

4.3.3. Traversability study

This last section addresses the compaction of the soil bins and the mobility of a vehicle on each soil bin. It bears mentioning that several methods have been evaluated for measuring the compaction of the soil, among others: Proctor compaction test and standard penetration test. However, those methods require large machinery (e.g rollers, rammers) and are only used in large civil-engineering tasks (e.g. roads, buildings, etc.). This has prevented us from finding a laboratory with the proper equipment for the relatively small soil bins assembled here (1x1x0.5 [m^3]).

Keeping in mind the small dimensions of the soil bins, which avoids the use of a full-size vehicle or robot, traversability was “quantified” by measuring the time that a scaled vehicle moved from two opposite corners in a soil bin. This way to quantify traversability is based on the loss of traction induced by slippage. This “loss of traction” eventually implies a higher time reaching a target position. More specifically, the time required to travel from A to B is higher as slip increases and is infinite when slip is 100%.

The vehicle used in these experiments was an RC car, which weights 0.43 [kg] and has pneumatic tires with a tread pattern. For each test, the RC car moved at a constant velocity by pulling the trigger in the transmitter to maximum power (full-throttle). The vehicle moved six times on the same bin. The traveling time was normalized following a known approach: $x' = (x-x^m/x^M-x^m)$, where x^m, x^M are the minimum and maximum values, respectively. In this case, the absolute traveling times varied between 1 and 5 [s], and the traveled distance was 0.9 [m].

Table 3 shows the traveling time of the scaled vehicle for each soil bin. The best “traversability”, less loss of traction, was observed in wet sand where the vehicle experienced neither slippage nor sinkage. A similar result was obtained in the sandy bin with a moisture content of around 12%. Gravel meant a proper mobility but a bumpy ride that sometimes led to embedding events. Bedrock caused some embedding events when the wheels moved over loose dry sand. Because of the cohesionless nature of the dry-sand bin (surface), the vehicle got stuck in all the experiments.

Observe that the grass bin has been excluded from this comparison. It was difficult to test the scaled vehicle with the vegetated terrain because the plants were taller than the wheels of the

vehicle and it got trapped. In any case, it has been previously demonstrated that the presence of vegetation in sandy soil means the soil is stabilized and leads to an efficient traversability of full-scale vehicles. For that reason, the vegetated-soil bin has been considered the second-best scenario in this work after wet sand.

Table 3
Traveling time for each experiment. Notice that the columns show the traveling time normalized between 0 and 1; being 0 the case when the vehicle needs 1 [s] to travel 0.9 [m], and 1 when it requires 5 [s].

Soil bin/test number	#1	#2	#3	#4	#5	#6	Norm. time
Dry sand	∞	∞	∞	∞	∞	∞	∞
Wet sand	0.02	0	0	0	0	0.02	0.01
Sand	0	0.12	0.20	0	0	0.20	0.09
Bedrock	0.52	0.30	0.50	0.52	0.72	0.95	0.59
Gravel	0.77	1	0.27	0.50	0.52	0.80	0.64

4.4. Results

This section describes the field tests performed to measure the evolution of the surface temperature and to derive thermal inertia. The first four sections analyze the experiments in terms of the temperature measured by the thermal camera and the other variables measured with the sensors and weather stations.

The following emissivity values have been considered in this work: dry sand 0.92, wet sand 0.95, gravel 0.90. The value for bedrock has been obtained taking into account the mixed composition of this bin (dry sand and rocks), eventually, a value of 0.93 has been selected. The emissivity of grass has been selected as 0.98, according to the authors' experience for similar vegetated terrains. Another key element related to the calculation of thermal inertia is the albedo. According to the Kirchhoff's law of thermal radiation for an arbitrary body emitting and absorbing thermal radiation in thermodynamic equilibrium, the emissivity is equal to the absorptivity. This result leads to the following relation: $A = 1 - \varepsilon$, where A is albedo and ε is emissivity.

Finally, it bears mentioning that the surface temperature derived from the thermal camera has been obtained as the average value of the whole surface of the soil bin (see rectangles in Figure 2). An interesting video showing a 24-hour cycle of thermal and visual images is available at: http://web.mit.edu/mobility/videos/thermal_camera_24hour.mp4.

4.4.1. Experiment 1. Clear sunny day

Figure 31a shows the surface temperatures obtained using the thermal camera. Observe a typical 24-hour cycle where the temperature drops and then increases one hour after sunrise (7am). After that, the temperature increases and drops again at dusk. This plot demonstrates the key role of moisture content in the variation of the temperature. In fact, the body with the smallest variation is the wet-sand bin. Observe, in Figure 4c, that the wet sand has a moisture content between 15-20% during this 24-hour cycle. Special mention must be made of the fact that moisture content has been kept within the desired threshold by manual watering.

It bears mentioning that the highest differences among the soils appear from 10 am to 8 pm. This means the capacity of discrimination is mostly valid during the day.

Figure 31b shows that the difference dry-wet sand is high during the day because water cools the surface of the wet-sand bin. It is not altogether unexpected to see that the difference between dry sand and bedrock is very small because bedrock is mainly composed of fine sand. Gravel is always hotter than dry sand. There are two key factors that might explain this result: (1) wind cools more easily the small grains of sand than the small stones of gravel; (2) gravel is composed of almost black stones and sand is composed of bright tiny grains. Dark materials mean a smaller reflectivity (or higher absorptivity), and hence, they get warm more easily. Finally, gravel is always hotter than bedrock because the (bright) rocks in the bedrock bin are colder than the smaller stones in gravel.

The temperatures obtained with the probes submerged in the bins are displayed in Figure 31d. These results validate the temperature profiles obtained with the thermal camera. Obviously, slight differences are observed because those probes are submerged at 0.01 [m] below the surface. In particular, different dynamics and heat fluxes may occur (evaporation, wind, humidity, etc.).

Finally Figures 31e, 31f deal with weather variables: relative humidity, wind speed, solar irradiance, and air temperature. These plots demonstrate that this experiment was performed during a mild day with moderate wind speeds (0.4 - 2.8 [m/s]), and a clear day with no clouds: solar irradiance from 0 to 1,000 [W/m^2] and from 1,000 to 0 [W/m^2] with no significant disturbances.

4.4.2. Experiment 2. Cloudy and rainy day

Figure 32a displays the result during a rough day with cloudy periods and a heavy rain and strong wind during the central part of the day. This experiment demonstrates that the temperature measured with the thermal camera (top layer) is always higher than the temperature of the subsurface when there is a high sun irradiance (clear sky), see Figure 32d. However, when the sun is not shining (clouds and rain) the temperature of all the soil bins becomes similar, see Figure 32b. When the sun heats the bins after the rain, there is again a noticeable difference in the surface temperatures. A similar behavior is observed regarding the temperature of the sensors submerged in the soils.

An interesting behavior appears regarding the moisture content of both the wet-sand and dry-sand bins. Notice that even though it is raining from 12 pm to 3 pm the moisture content does not change, see Figure 32c. Recall that the moisture meters are at a depth of 0.2 [m] and perhaps the rain water evaporates at the surface of the bins. Even in the case of the wet sand, moisture drops until the human waters again at 3:30 pm. As in the previous experiment, a constant moisture content is ensured by manually watering the bin.

Finally, Figures 32e, 32f show the weather measurements. Especial mention is for Figure 32f where solar irradiance and temperature drops suddenly from 12 pm to 3:30 pm, that is, when the rainy event happened.

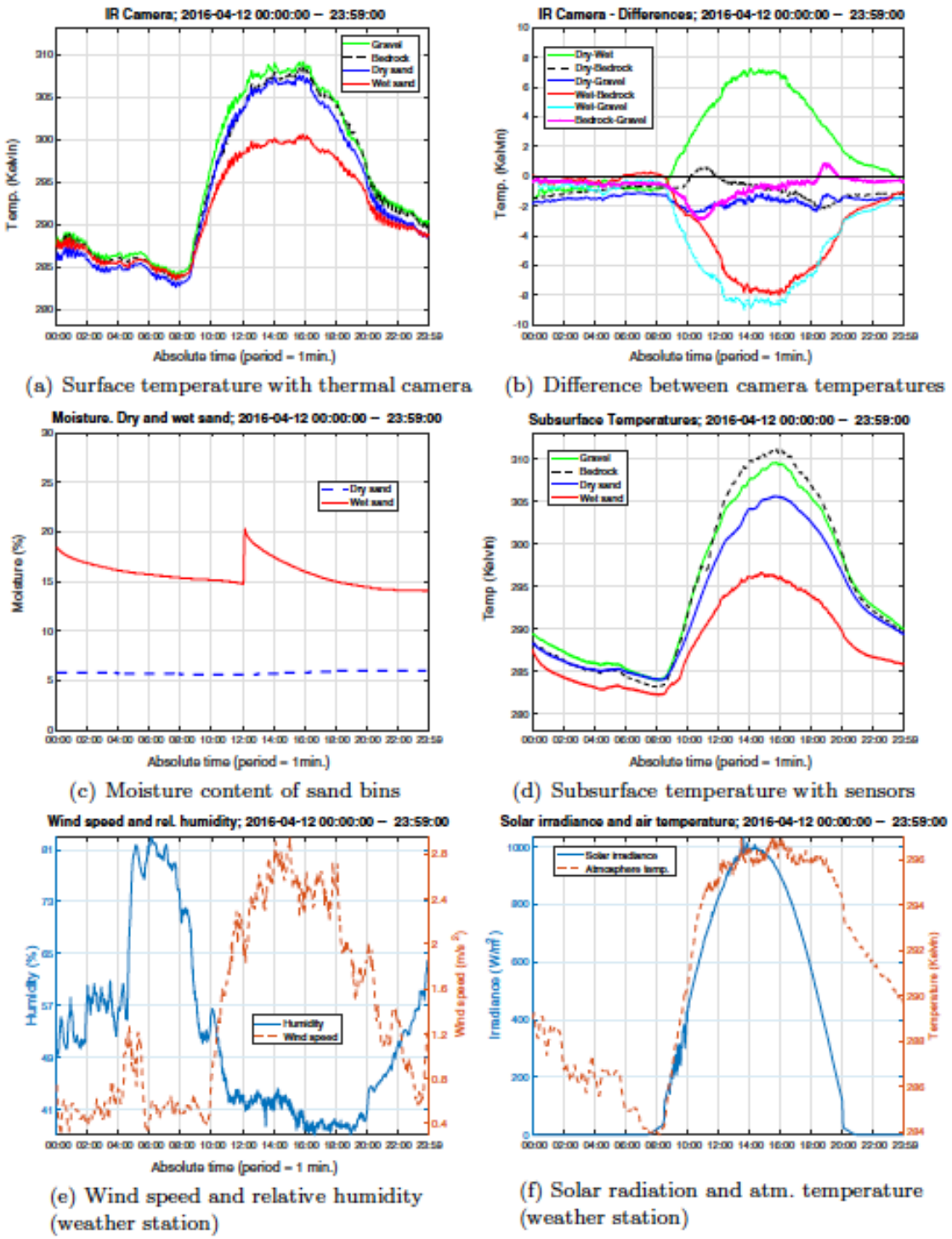

(a) Surface temperature with thermal camera

(b) Difference between camera temperatures

(c) Moisture content of sand bins

(d) Subsurface temperature with sensors

(e) Wind speed and relative humidity (weather station)

(f) Solar radiation and atm. temperature (weather station)

Figure 31. Experiment 1. Clear sunny day. Observe the major difference between the surface temperatures is in the morning and afternoon

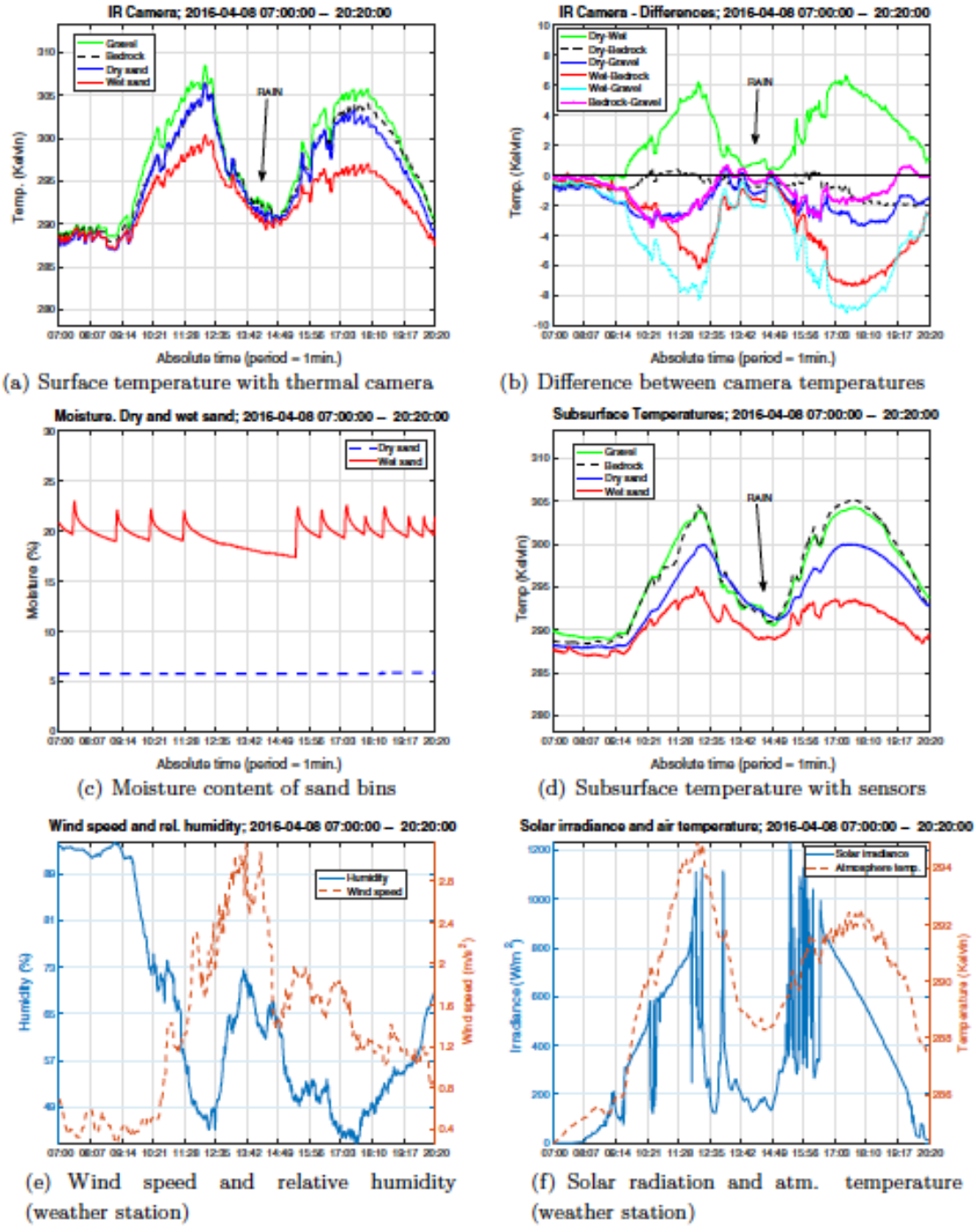

(a) Surface temperature with thermal camera

(b) Difference between camera temperatures

(c) Moisture content of sand bins

(d) Subsurface temperature with sensors

(e) Wind speed and relative humidity (weather station)

(f) Solar radiation and atm. temperature (weather station)

Figure 32. Experiment 2. Cloudy and rainy day. Notice that during the cloudy period the surface temperatures becomes similar

4.4.3. Experiment 3. Vegetated soil and artificial lighting system

This experiment is based on the second configuration of the testing site (grass, sand, gravel, bedrock). Additionally, the artificial lighting system previously described was switched on at night.

Figure 33 shows the behavior of the different soil bins during a 48-hour cycle. The first conclusion is that the temperature of the grass is similar to the profile observed in the wet-sand bin in previous experiments. However, two key variables are different here, the first one is that now a much hotter day is considered (irradiance > 1,000 [W/m^2]), and the second difference is that the moisture content of grass is almost one third of the one in wet sand (7% versus 20%). This result shows that vegetation cools a surface much more efficiently than water. Notice that some studies show that there is a correlation between the density of plants (leaf area index, LAI) and soil moisture. However, it is difficult to generalize such relation because it depends on several factors (e.g. atmospheric variables) and even on the soil type.

Another interesting conclusion is drawn after switching on the lighting system at night, see Figures 33a, 33b, 33c. Notice that the temperatures of the soil bins during the second night are slightly higher under similar weather conditions, Figure 33e, 33f. In any case, this difference is not big enough to ensure that this change is due to the lighting system, perhaps because the lamp was far from the bins (> 1.5 [m]).

4.4.4. Experiment 4. Using an artificial heating system at night

This last experiment intends to show if it is possible to discriminate the soils considered in this work at night. Recall that, after sunset the difference between the surface temperatures is small enough that prevents the discrimination between soils using the thermal camera.

Figure 34a shows the way to proceed in this experiment. Each soil bin is lit for 2 minutes with a 500-W artificial lighting system at a distance of 1 [m] approximately. Figure 34b shows the result for the second configuration of the testing site (grass, gravel, sand, bedrock). Observe that the surface temperature actually changes when it is heated by the lighting system. In particular, grass and bedrock change around 1 degree, and sand and gravel around 0.5 degrees. It bears mentioning that the change between measurements due to noise in the sensor is much smaller than these values (0.1-0.2 degrees).

This simple experiment demonstrates that there is a certain correlation between the heating time and the increment in the soil temperature, which may be used for discriminating soils. In any case, an improved lighting/heating system will be analyzed in the future together with the following variables: distance between the lighting system and the soils, the power of the lamp, and the exposure time.

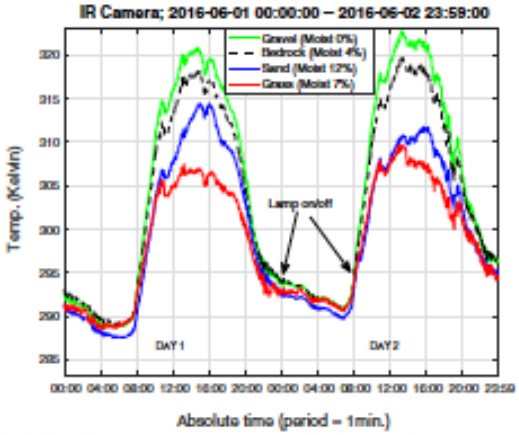

(a) Surface temperature with thermal camera

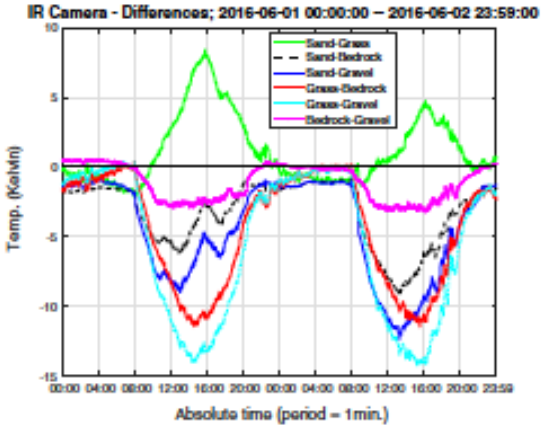

(b) Difference between camera temperatures

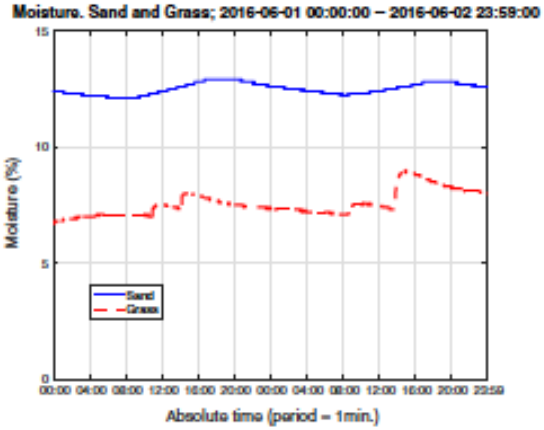

(c) Moisture content of sand and grass

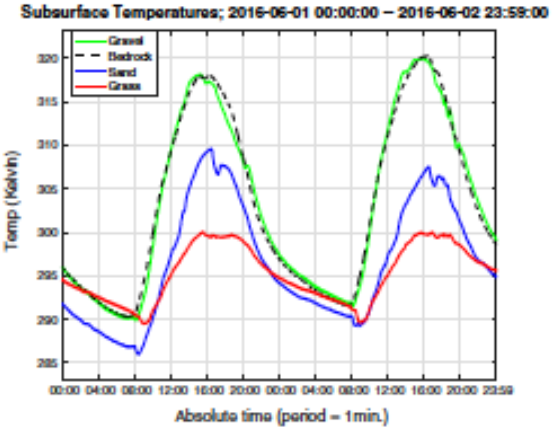

(d) Subsurface temperature with sensors

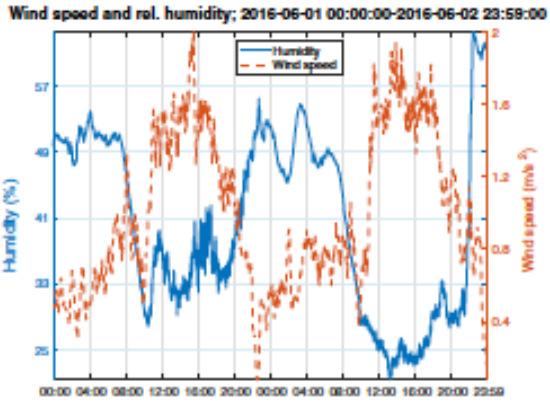

(e) Wind speed and relative humidity (weather station)

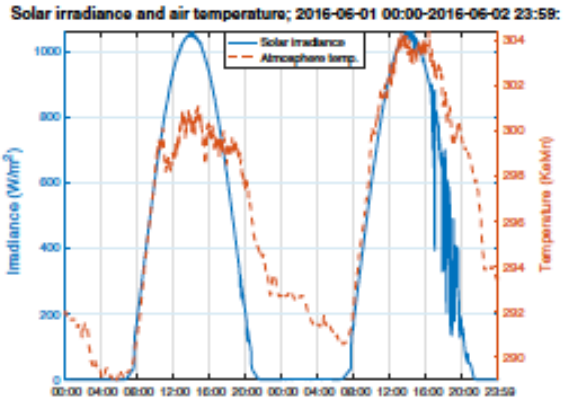

(f) Solar radiation and atm. temperature (weather station)

Figure 33. Experiment 3. Vegetated soil and artificial lighting system

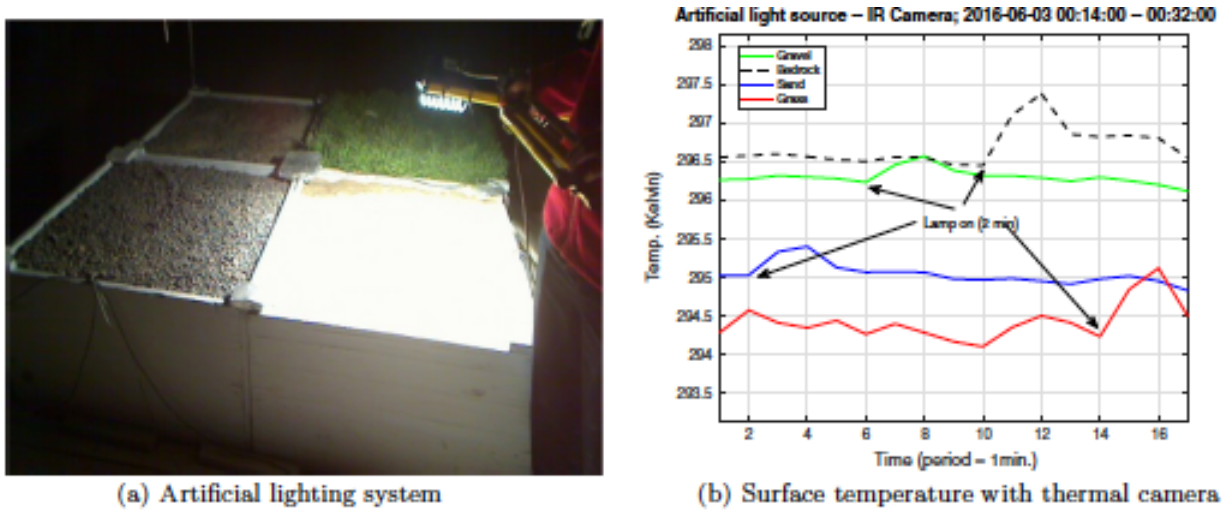

(a) Artificial lighting system (b) Surface temperature with thermal camera

Figure 34. Experiment 4. Heating a surface at night with an artificial lighting system. Observe that surface temperatures actually vary during the 2-minute exposure time

4.4.5. Correlation between thermal inertia, moisture, and traversability

This last section deals with the main contributions of this work, that is, the influence of soil moisture and vegetation on thermal inertia, and the relation between thermal inertia and traversability.

Figure 35a shows thermal inertia estimated for the sandy soils in relation to moisture content. Observe that even though all these surfaces are composed of the same basic material (i.e. sand), thermal inertia increases with soil moisture. A remarkable behavior is obtained with the vegetated soil. In this case, a similar thermal inertia to wet sand is obtained even though the moisture content is almost one third of wet sand.

Recall that thermal inertia is related to the compaction of a surface, and compaction with traversability. Traversability comprises a key variable for controlling a mobile robot in off-road conditions. In this context, Figure 35b constitutes the second major contribution of this work. Observe that there is a relation between traversability and thermal inertia. In addition to that, this result shows that the surfaces with the highest thermal inertia, wet sand and grass, also mean the most traversable/compact terrains. Recall that high traversability implies low embedding risk (i.e. low slippage) and poor traversability may lead to untraversable routes (i.e. high slippage).

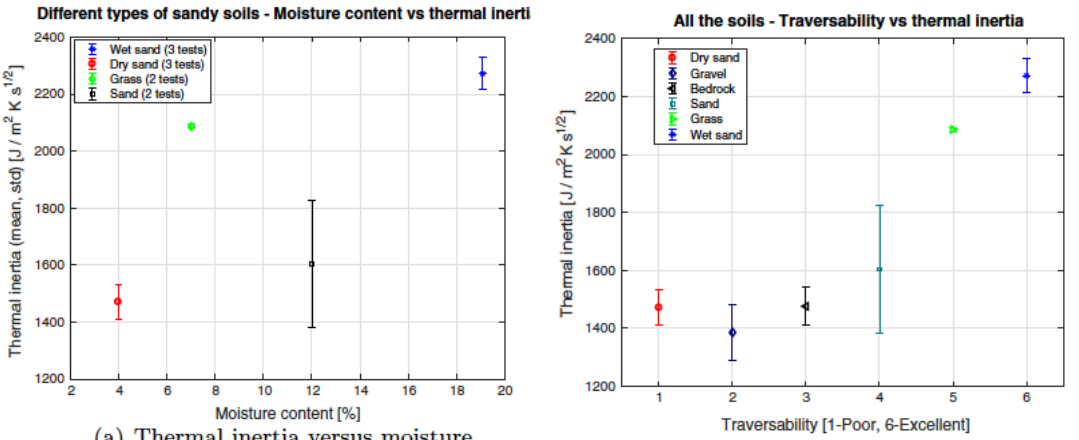

(a) Thermal inertia versus moisture content for the sandy soils

(b) Thermal inertia versus traversability

Figure 35. Quantitative analysis of thermal inertia. Observe the relation between thermal inertia and moisture content, and between thermal inertia and traversability (poor traversability means high slippage, and excellent traversability implies no slippage)

4.5. Discussion

Heat and moisture fluxes from the surface to the atmosphere are controlled by turbulent transfer processes which depend on various factors: wind speed, surface roughness, atmospheric temperature, and relative humidity. Because of the complexity of this process and the limitations of estimating thermal inertia from thermal vision this work does not aim to contribute a quantitative and accurate method for discriminating soils. However, this work does contribute a proper methodology for using lightweight thermal cameras (onboard vehicles) to identify those soils where thermal inertia is higher than others, which may mean a higher moisture content and a superior traversability.

This work demonstrates that discrimination between wet-sand, dry-sand, and vegetated areas is possible by means of thermal vision. Dry sand deals with cohesionless soils (no water wetting the soil). Due to this loose nature, dry sand is usually avoided as there is a high risk of vehicle entrapment. On the other hand, wet sand and vegetation would probably imply more compact soils, higher cementation, and hence, more appropriate for robot motion. However, it is also important to remark that when the moisture content of a soil is up to the optimum moisture content (or maximum dry density) of such soil, compaction is adversely influenced. This fact highlights that thermal signature or thermal inertia maybe is not enough to identify the optimal compact state of wet sand. In any case, future research will be performed with a broader set of moisture levels (from dry sand to mud) to validate the previous statement.

As observed in the previous experiments, discrimination between soils is only advisable during the day. Recall that at night the temperature difference between the soil bins is almost zero. More specifically, the difference is within 2 degrees from 12 am to 8 pm. This result highlights an important controversy to the traditional advantage of thermal cameras, that is, night operation. For that reason, a second set of experiments have been carried out using an artificial lighting system. This preliminary solution shows that discrimination between soils can be achieved by

means of a trade-off between the power of the artificial lighting system, the exposition time, and the distance to the soil.

4.6. Conclusions and future work

Thermal cameras constitute a remarkable perception system for off-road mobile robots and autonomous ground vehicles. This work means an initial investigation focused on the challenges associated with the use of thermal cameras in wet and vegetated soils, and shows how thermal properties actually depends on the moisture content and the relation between those thermal properties and traversability. As a proof of concepts, traversability is understood in terms of the loss of traction and the traveling time of a scaled vehicle moving over the soil bins.

This work benefits from the simple model that estimates the apparent thermal inertia. In any case, future research will concentrate on solving the more complicated heat transfer model as well as validating the derived thermal inertia with ground-truth values. In addition to that, future efforts will address the determination of thermal inertia over short periods of time (e.g. 1 minute or 2 minutes) instead of the current 24-hour cycle. That research will benefit from the preliminary results obtained here with the artificial lighting system with 2-minute cycles.

Observe that one key limitation of the use of thermal cameras for terrain traversability is that they detect features associated with the upper few centimeters of a surface. However, terrain traversability is also dictated by the layer below the topmost terrain surface. In this sense, thermal cameras may be complemented with other sensors (e.g. ground penetrating radars).

Finally, a comprehensive analysis will be run in order to determine the traversability of an actual vehicle moving over the considered soils. This step will enable closed-loop control of mobile robots in off-road conditions predicting terrain traversability by means of a thermal camera.